

Optical and thermal characterization of a group-III nitride semiconductor membrane by microphotoluminescence spectroscopy and Raman thermometry

Mahmoud Elhajhasan, Wilken Seemann , Katharina Dudde, Daniel Vaske, and Gordon Callsen *

Institut für Festkörperphysik, Universität Bremen, Otto-Hahn-Allee 1, 28359 Bremen, Germany

Ian Rousseau, Thomas F. K. Weatherley, Jean-François Carlin, Raphaël Butté , and Nicolas Grandjean

Institute of Physics, École Polytechnique Fédérale de Lausanne (EPFL), CH-1015 Lausanne, Switzerland

Nakib H. Protik

Institut für Physik und IRIS Adlershof, Humboldt-Universität zu Berlin, 12489 Berlin, Germany

Giuseppe Romano

MIT-IBM Watson AI Lab, 314 Main St., Cambridge, Massachusetts 02141, USA

 (Received 30 June 2023; revised 9 October 2023; accepted 13 November 2023; published 29 December 2023)

We present the simultaneous optical and thermal analysis of a freestanding photonic semiconductor membrane made from wurtzite III-nitride material. By linking microphotoluminescence spectroscopy with Raman thermometry and other spectroscopic techniques, we demonstrate how a robust value for the thermal conductivity κ can be obtained using only optical noninvasive means. For this, we consider the balance of different contributions to thermal transport given by, e.g., excitons, charge carriers, and heat-carrying phonons. In principle, all these contributions can be of relevance in a photonic membrane on different length scales. Further complication is given by the fact that this membrane is made from direct band gap semiconductors, designed to emit light via an $\text{In}_x\text{Ga}_{1-x}\text{N}$ ($x = 0.15$) quantum well embedded in GaN. Thus, III-nitride membranes similar to the one of this study have already been successfully used for laser diode structures facing thermal limitations. To meet these intricate challenges, we designed an experimental setup that enables the necessary optical and thermal characterizations in parallel. After the optical characterization by microphotoluminescence, we follow a careful step-by-step approach to quantify the thermal properties of our photonic membrane. Therefore, we perform steady-state micro-Raman thermometry, either based on a heating laser that also acts as a probe laser (one-laser Raman thermometry), or based on two lasers, providing the heating and the temperature probe separately (two-laser Raman thermometry). For the latter technique, we can obtain temperature maps over several hundreds of square micrometers with a spatial resolution less than $1\ \mu\text{m}$. As a result, the temperature probe volume using the two-laser Raman thermometry technique can be increased by a factor exceeding 100 compared with the conventional one-laser Raman thermometry technique, which impacts the derivation of the thermal conductivity κ . Only based on our largest temperature probe volume we derive $\kappa = 95_{-7}^{+11}\ \text{W m}^{-1}\ \text{K}^{-1}$ for the c plane of our $\approx 250\text{-nm}$ -thick photonic membrane near room temperature, which compares well to our *ab initio* calculations, applied to a simplified structure, yielding $\kappa = 136\ \text{W m}^{-1}\ \text{K}^{-1}$. Based on these calculations, we explain the particular importance of the temperature probe volume, as quasiballistic transport of heat-carrying phonons, which is of high relevance for determining κ , occurs on length scales beyond the penetration depths of the heating laser and even its focus spot radius. The one-laser Raman thermometry technique, therefore, fails to derive realistic κ values, unlike the two-laser Raman thermometry that can probe temperatures over sufficiently large volumes. The present work represents a significant step towards the achievement of noninvasive, highly spatially resolved, quantitative thermometry maps on a photonic membrane made of a direct band gap semiconductor, which is of particular relevance for photonic applications.

DOI: [10.1103/PhysRevB.108.235313](https://doi.org/10.1103/PhysRevB.108.235313)

I. INTRODUCTION

The optical properties of semiconductors are extensively studied and are therefore becoming increasingly well understood over the full size variation, from bulk crystals down to nanostructures. Measuring fundamental optical phenomena such as absorption, reflectivity, light scattering, and photoluminescence (PL) on various length- and timescales has nowadays become a widespread capability in many laboratories.

*gcallsen@uni-bremen.de

The nanostructures commonly in scope encompass the entire dimensionality range from quantum dots (zero dimension or 0D), over nanowires (one dimension or 1D), to quantum wells (two dimensions or 2D). Consequently, a wide range of prototypes and devices was realized, scaling from, e.g., light detectors [1] over sensors [2] to light-emitting [3] and laser diodes [4]. For instance, laser-diodes often utilize nanostructures such as quantum wells (QWs) as a built-in light sources [5,6]. However, the high level of sophistication reached for the analysis of the photonic properties of these structures [7–9] is often contrasted by a limited understanding of the interfering thermal phenomena [10]. Commonly, either the photonic or the thermal properties of micro- and nanostructures are studied, while the interrelation of both phenomena is rarely reported [11,12], prohibiting any future mutual optimization. So far, a link between photonic and phononic properties has been established in the field of nano-optomechanics, focusing mostly on low-frequency phonons (MHz to GHz range) [13]. However, thermal transport represents an even more intricate phenomenon that can be mediated by a weighted balance of, e.g., charge carriers [14,15], excitons [16], and most prominently high-frequency, thermal phonons up to the THz range [17].

Before any link between optical and thermal material properties can be studied, one first has to develop a robust experimental technique that enables such studies. Clearly, any interlinked understanding of optical and thermal material properties could potentially pave the way towards mutual optimizations. Established thermal characterization techniques such as, e.g., 3ω measurements [18] are not straightforwardly compatible with photonic micro- and nanostructures for size reasons and the required fabrication of metal contacts. A similar observation seems valid for time-domain thermal reflectance (TDTR) measurements [14,19] as another established thermal characterization approach, which most frequently relies on metal transducers. Purely thermally induced reflectivity changes in semiconductors are generally considered small over wide energy ranges, if not located in close energetic vicinity to electronic and excitonic resonances [20,21]. Thus, in practice metal transducers with larger thermorefectance coefficients in the wavelength range of interest are commonly required for TDTR measurements [22,23]. The processing of such metal transducers can potentially deteriorate photonic structures. Therefore, a fully noninvasive thermal characterization technique is required, which in the best case can readily be combined with standard optical analyses such as absorption and reflectivity measurements, as well as (time-resolved) PL spectroscopy. In a best-case scenario, this thermal characterization technique should also feature diffraction limited spatial resolution similar to, e.g., micro-TDTR [24], together with a large applicable temperature range and sufficient temperature resolution. Certainly, for many applications any optical and thermal characterization at room temperature and beyond would be sufficient. Nevertheless, most interesting thermal transport physics connected to, e.g., the occurrence of various thermal phonon transport regimes, would also motivate thermometry down to cryogenic temperatures [25–27]. In summary, a quantifying thermal characterization technique with excellent integrability, high spatial resolution, as well as a wide operating

temperature range and sufficient temperature resolution is desired.

Raman thermometry appears as a promising thermal characterization technique in the light of these requirements [28–30]. Raman measurements cannot only be performed in a micro-PL (μ PL) setup, one can also directly map micro-Raman (μ Raman) spectra with a spatial resolution close to the diffraction limit [28] over a wide range of temperatures. However, these promising aspects of Raman thermometry pair with a number of challenges, whenever the Raman laser is not exclusively used as a temperature probe to map, e.g., the Joule heating of a transistor structure under operating conditions [31]. As soon as the Raman laser is simultaneously used for the sample heating and the temperature probing based on Raman spectra, the situation gets more complicated [30,32]. The applied laser heating challenges the data analysis in contrast with, e.g., common 3ω or TDTR measurements that apply Joule heating to a semiconductor via metal contacts or transducers. In general, the thermal resistance of the metal-to-semiconductor interface represents a manageable challenge for 3ω and TDTR experiments and directly correlated thermal simulations [19]. In contrast, for Raman thermometry, depending on the light penetration depths of the heating laser, one has to either model the laser heating by a semiconductor surface heating or a fully volumetric heating, which requires precise knowledge of the absorption coefficient and its wavelength dependence [30,33]. Even more severe, in stark contrast to the Joule heating via metalized semiconductor surfaces, the above band gap optical excitation of semiconductor samples by a suitable heating laser can excite charge carriers [14,15] or even generate optical excitations such as excitons [16] and exciton-polaritons [34]. As a result, not only thermal phonons are generated, but all these additional fundamental excitations, which diffuse away from the laser-induced heat spot. This situation is then further complicated by the optical decay of, e.g., excitons and exciton-polaritons during their propagation. Any measured temperature rise in a semiconductor that is directly induced by laser heating (i.e., without a metal transducer) is challenged by all these additional energy transport mechanisms. Commonly, with thermal phonons we refer to high-frequency heat-carrying phonons that predominantly contribute to thermal transport at all temperatures in the scope of the present work. For the sake of completeness, radiative heat transfer and related near-field phenomena [35] can also be added to the list of these mechanisms. However, these mechanisms can safely be neglected in the present work due to the temperature differences and distances involved as well as the dominant contributions of phononic thermal transport.

Consequently, Raman thermometry that relies on laser heating can only lead to a solid thermal characterization of a semiconductor if its optical properties are thoroughly studied in-parallel. Not only the absorption must be known [29], but also the overall quantum efficiency of the sample is required for an estimation of how much of the absorbed light contributes to the heating of the sample. Here, the fact that common Raman thermometry applies the same laser for laser heating and temperature probing represents a strong limitation because the electronic [36] or thermal excitations [37] connect to different characteristic mean-free path lengths. Thus, such one-laser Raman thermometry (1LRT) technique

is best extended to two-laser Raman thermometry (2LRT), by transferring the role of the temperature probe to a second laser, which can be scanned away from the laser heat spot, over the entire structure of interest. Based on temperature maps extracted from Raman map scans, it is consequently possible to observe temperature distributions that are caused by a weighted balance of the different mechanisms contributing to thermal transport. Thus, as the related mean-free path lengths vary, 2LRT measurements have the potential to disentangle different contributions to thermal transport by varying the distance between the temperature probe and the laser-induced heat spot. Initially, Hsu *et al.* applied 2LRT measurements to carbon nanotubes [38] while the demonstration of its applicability to silicon membranes [39] and polycrystalline nanomembranes of MoS₂ [40] was also shown. However, all existing experimental 2LRT setups, as described in detail by Reparaz *et al.* [39], require full optical access from the sample front- and backside to overlap the heating and the probe laser focus spots on the sample. While such an approach is still feasible, e.g., for microstructured silicon membranes [41], most photonic micro- and nanostructures can only be accessed from one side because a full substrate removal is often detrimental for delicate photonic structures [10,42,43].

In this contribution we apply 1LRT and 2LRT to a photonic membrane structure, which has widely been described in the literature [10,42–46]. This membrane is mostly made from GaN and incorporates an In_xGa_{1-x}N ($x = 0.15$) quantum well (QW) as built-in light source. Structures very similar to this photonic membrane have already formed the basis for publications reporting on, e.g., one-dimensional nanobeam lasers [10,43] and two-dimensional photonic crystals [42] with excellent optical properties. Vico Triviño *et al.* reported on record-low-threshold blue lasing of InGaN/GaN nanobeam lasers [43], which were based on the photonic membrane also used for the present work. As such photonic structures can experimentally be accessed only from one side, a fully customized 1LRT and 2LRT setup was constructed, which allows heating and probing sample temperatures from the same side by combining conventional micro-Raman mapping and a laser scanner. To highlight the functionality of this setup, all experimental results are introduced in a careful step-by-step approach, aiming to achieve quantitative Raman thermometry despite the numerous challenges posed by a photonic membrane made from direct band gap semiconductor material. This also includes in-parallel an analysis of the PL signal, aiming to discard any impact of free carriers and excitons on our determination of the thermal conductivity κ . We show that, based on 1LRT or 2LRT measurements, one can determine strongly different thermal conductivities, which are linked to the different temperature probe volumes. 1LRT measurements are not ideally suited for a quantitative determination of κ in our membranes, whereas 2LRT measurements yield $\kappa = 95_{-7}^{+11} \text{ W m}^{-1} \text{ K}^{-1}$ for our ≈ 250 -nm-thick photonic III-nitride membrane. We then compare κ values derived from *ab initio* calculations to our experimental results, while analyzing the dependence of the related cumulative κ on the phonon mean-free path lengths l^{MFP} provides an explanation for the different experimental results derived from 1LRT and 2LRT measurements. Thus, only 2LRT measurements allow for a truly thermal quantitative analysis of our photonic III-nitride

membrane, providing a strong motivation for any future application of this experimental technique.

The paper is structured as follows: In Sec. II, we first introduce the photonic membrane made from III-nitride material (Sec. II A) that we optically (μ PL) and thermally (Raman thermometry) characterize based on our customized optical setup (Sec. II B). Herein, we describe the mode of operation of our optical setup in a four-step-process, which gradually raises the level of complication for our measurements. This rigorous step-by-step approach starts with Step A, the presentation of the μ PL spectroscopy in Sec. III. Subsequently, in Sec. IV the precharacterization of our photonic membrane is complemented by spatially resolved, nonresonant and selected resonant Raman measurements on GaN, which constitutes Step B in our hierarchy. Such resonant and nonresonant Raman spectroscopy represents the basis for the Raman thermometry described in Sec. V, which is not yet spatially resolved (Step C). This section is subdivided into Secs. V A and V B, which introduce the 1LRT and the 2LRT₀ measurements without any spatial displacement between the heat and the probe lasers. Herein, we also introduce our numerical simulations that allow us to extract κ from our 1LRT and 2LRT without spatial displacement (2LRT₀) measurements. Based on these experimental and numerical foundations from Secs. II–V, we can turn towards the last Step D in Sec. VI that describes 2LRT measurements. Here, we show our temperature map scans that enable the determination of κ , which is additionally modeled in Sec. VII based on state-of-the-art *ab initio* calculations. As we experimentally find a particular scaling behavior between the κ values derived from 1LRT, 2LRT₀, and 2LRT measurements, we discuss this observation in Sec. VIII based on our theoretical findings from Sec. VII. Finally, we present our discussion and the outlook in Sec. IX, before summarizing our results in Sec. X. In addition to this paper, more technical details and concepts are further described in the Supplemental Material (SM) [47] in the Supplemental Secs. (S-Secs.) I–IV (see also Refs. [48–53] therein).

II. EXPERIMENTAL DETAILS

The overall structure of the photonic membrane is introduced in Figs. 1(a)–1(d). In addition, a simplified sketch of the experimental setup that enables μ PL spectroscopy (optical characterization) in parallel with one-laser- and two-laser-Raman spectroscopy (thermal characterization) is given in Fig. 1(e). A more detailed drawing and explanation of the experimental setup can be found in S-Sec. I [47].

A. The photonic membrane

The layer stack that forms the basis for the photonic membrane is made from *c* plane wurtzite AlN, GaN, and In_xGa_{1-x}N ($x = 0.15$) grown on an *n*-type (111) silicon substrate as sketched in Fig. 1(a). Such material growth on silicon (111) is key to the formation of a membrane structure, as silicon can be selectively etched. The group-III nitride material was grown by metal-organic vapor phase epitaxy (MOVPE) in a horizontal Aixtron 200/4 RF-S low pressure reactor and details regarding the growth of such epilayers on silicon (111)

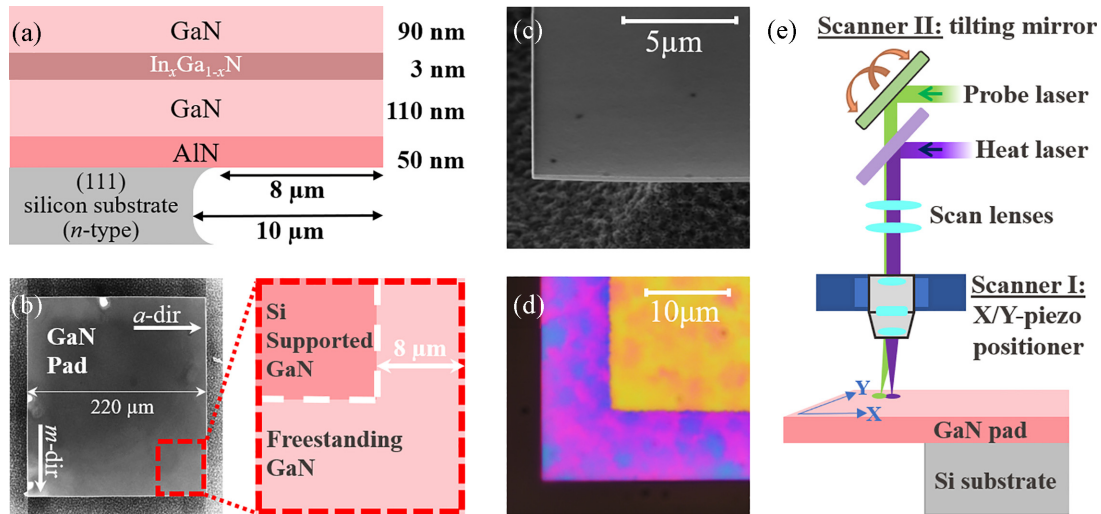


FIG. 1. (a) Layer sequence of the photonic membrane made from group-III nitrides grown on n -type silicon (111). The origin of the layer sequence is explained in the main text. (b) Top-view SEM image of the photonic membrane that mainly consists of c -plane GaN. The a - and m -plane crystal directions are indicated. The dashed red rectangle along with the sketch on the right indicates the freestanding part of the photonic membrane in one of its corners, which extends up to a width of $\approx 8 \mu\text{m}$. (c) Top-view SEM image of the photonic membrane illustrating the underetch, the roughened silicon substrate, and the photonic GaN membrane. (d) Top-view light microscope image of the same corner region of the photonic membrane. Here, the color fluctuations indicate thickness fluctuations of the photonic membrane. (e) Simplified sketch of the experimental two-laser setup that enables micro-photoluminescence spectroscopy (optical characterization) in parallel to one-laser- and two-laser-Raman spectroscopy (thermal characterization) based on continuous wave lasers.

can be found in Ref. [54]. First, 50 nm of AlN were deposited on silicon (111) to avoid melt-back etching [55]. Afterwards, 110 nm of GaN, the 3-nm-thick $\text{In}_x\text{Ga}_{1-x}\text{N}$ ($x = 0.15$) QW, and finally another 90 nm of GaN were grown. Here, the QW is deliberately placed 10 nm above the geometric center of the surrounding GaN, taking into account the lower refractive index of AlN [46]. This way, the coupling of this built-in light source to the fundamental electromagnetic mode is enhanced. The overall membrane thickness of ≈ 250 nm is larger than required for single electromagnetic mode operation of this membrane, which is of relevance as soon as, e.g., a photonic crystal is processed for the blue spectral range [46]. However, this represents a trade-off, aiming to achieve the smoothest possible GaN surface without pits or cracks. The entire stack of III-nitride material is not intentionally doped and the GaN material exhibits a free carrier concentration of $3 \times 10^{16} \text{ cm}^{-3}$. Detailed secondary ion mass spectrometry of the photonic membrane can be found in Ref. [46], showing that the main impurities in our photonic membrane are silicon and carbon with concentrations of $\approx 3 \times 10^{16}$ and $\approx 5 \times 10^{16} \text{ cm}^{-3}$.

The need of smooth surfaces for photonic applications [44] is also beneficial for the in-plane thermal transport that is studied in this work. To quantify light scattering losses in group-III nitride photonic crystals in the blue spectral range, Rousseau *et al.* [44] have conducted detailed atomic force microscopy (AFM) on the front- and backside of precisely the membrane that is studied in the present work. After all required processing steps to form the photonic membrane, they determined a GaN root mean square (rms) top surface roughness of 1.4 nm, whereas the AlN backside exhibited a rms roughness of 0.6 nm, which was extracted from $500 \times 500 \text{ nm}^2$ AFM scans. The backside roughness of the nitrogen-polar AlN was accessed by exfoliation and subse-

quent flipping of a large ($\approx 80 \times 80 \mu\text{m}^2$) square of an entire membrane similar to the GaN pad shown in Fig. 1(b). In addition to this surface roughness, a minor waviness was observed for the particular membrane in $25 \times 25 \mu\text{m}^2$ AFM scans, which yields a rms waviness of 4.9 nm and ≈ 30 nm peak-to-valley height variation over distances of 5–10 μm . These height variations lead to the color contrast shown in Fig. 1(d) due to thin-film interference. In addition, the AFM scans on the AlN surface on the backside of the photonic membrane yielded a high density of pin pricks forming dips that correspond to dislocations with a density of $3\text{--}4 \times 10^{10} \text{ cm}^{-2}$, which is a typical value for AlN grown on (111) silicon [56]. Similar AFM scans of the top GaN layer yield the same range for the dislocation density, which corresponds to a distance of 50–60 nm between these defects. For the sake of simplicity, in the following the epilayer from Fig. 1(a) will be described as the GaN pad (with silicon support) or membrane (without silicon support), as its main constituent GaN will dominate the thermal properties that lie in the scope of this work.

The processing that leads to the GaN pad structure illustrated in the scanning electron microscopy (SEM) image from Fig. 1(b) is based on electron-beam lithography, dry etching, and chemically selective vapor phase etching. First, hydrogen silsesquioxane is applied as negative tone resist for the electron-beam lithography, which also acts as a hard mask, enabling the transfer of written patterns into the underlying epilayer via dry etching. Exactly during this pattern transfer, any potential edge roughness of the etch mask is transferred to the underlying epilayer. As no apparent edge roughness can be observed within the spatial resolution limits of the applied electron microscope, only an upper bound for the rms sidewall roughness of $\lesssim 5$ nm can be estimated. It should be noted that this sidewall roughness does not represent a

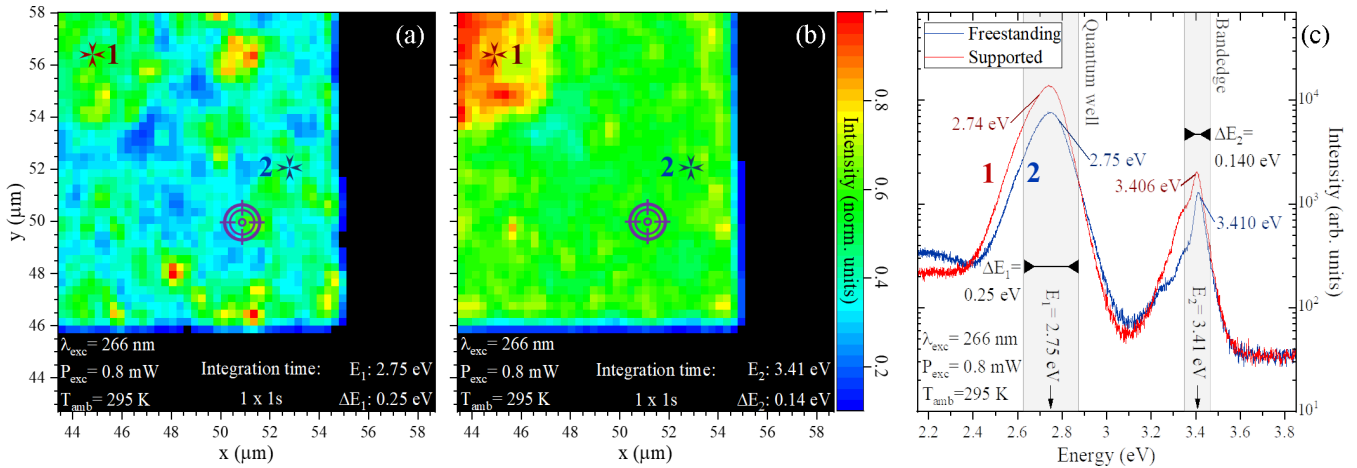


FIG. 2. Characterization of the photonic membrane by μ PL spectroscopy at an ambient temperature $T_{\text{amb}} = 295$ K under excitation with a cw UV laser with a wavelength $\lambda_{\text{exc}} = 266$ nm at a power $P_{\text{exc}} = 0.8$ mW. (a) Intensity distribution of the QW emission centered around $E_1 = 2.75$ eV with a bandpass $\Delta E_1 = 0.25$ eV, aiming to approximate the FWHM of the QW emission. Here, monolayer thickness and indium content fluctuations lead to intensity variations, which prominently appear as localization centers in the map scan. (b) In contrast, the GaN band-edge emission near $E_2 = 3.41$ eV shows a more homogeneous intensity distribution in the region of the freestanding GaN membrane with a bandpass matching its FWHM ($\Delta E_2 = 0.14$ eV). Here, the out-coupled signal strength only significantly rises in the top left corner, where the underlying silicon support structure begins, cf. Fig. 1(b). The target cross in panels (a) and (b) indicates the final desired position of the heating laser. (c) Comparison of two local μ PL spectra recorded at the color-matched indicators in panels (a) and (b).

general limit as even atomically flat sidewalls can be achieved by anisotropic wet etching of GaN by tetramethylammonium hydroxide [57]. To this end, the corresponding sidewalls of any etched structure must be aligned to the crystallographic axes, as it is the case for the present GaN pad, cf. Fig. 1(b). The edge region of this GaN pad is then released from the silicon substrate over ≈ 8 μm by chemically selective vapor phase etching using XeF_2 . The resulting structural situation is sketched in Fig. 1(b) and further detailed by the SEM image from Fig. 1(c). Additional details regarding the sample growth and processing can be found in Ref. [46] and the Supplemental Material of Ref. [44], reporting on high-quality one-dimensional photonic crystal cavities based on the epilayer in use for the present work. For comparison, we also perform 1LRT measurements on a freestanding piece of a state-of-the-art *c*-plane GaN wafer with a dislocation density $\approx 10^6$ cm^{-2} , which already formed the basis for detailed optical studies on InGaN-based light-emitting diodes [58].

B. The customized optical setup

Figure 1(e) introduces the spectroscopic setup that enables spatially resolved μ PL and μ Raman map scans by the independent displacement of two laser spots on the surface of the epilayer. Whereas the basic features of this setup are described in the following, its full description is given in S-Sec. I [47]. First, an ultraviolet (UV) laser that provides above band gap excitation of GaN (purple), is guided towards the sample via a suitable beam splitter and a microscope objective. We use either a 266 or a 325 nm continuous wave (cw) laser for this purpose. Both lasers can then directly be used as excitation lasers for μ PL spectroscopy. The excitation spot of both lasers can be translated across the surface of the GaN pad over a range of ≈ 100 μm by actuating the closed-loop

X-Y piezo stage labeled as scanner I in Fig. 1(e). In addition, coarser movements of the entire sample structure are enabled by a long-range X-Y-Z piezo stage (not shown) that holds the sample in a cryostat, where it is held at a base pressure of $\approx 1 \times 10^{-6}$ mbar. Even though the cooling option of this cryostat with its built-in X-Y-Z piezo stage is not in use for the present work, it still acts as the heat sink for the entire sample, keeping it at an ambient temperature of $T_{\text{amb}} = 295$ K. Upon UV excitation, the resulting μ PL signal is guided backwards through the microscope objective towards the detection system comprising a suitable monochromator and charge-coupled device (CCD) detector with a spectral resolution of ≈ 1 cm^{-1} in the visible region around 532 nm.

Resonant Raman spectra based on one of the cw UV lasers (266 nm or 325 nm) are measured in the same manner. Here, varying the power of these cw lasers gives direct access to Raman thermometry based on one laser (1LRT), which originates the labeling of these lasers as “heating lasers.” However, low signal strength in addition to the underlying μ PL signal arising from various optical transitions in GaN can significantly challenge the data recording as further detailed in Sec. IV A. In addition, nonresonant Raman map scans of the epilayer can be recorded based on two visible (VIS) cw lasers (488 nm and 532 nm), which we describe as probe lasers. Therefore, any movement of the visible laser spot can either be achieved by scanner I or the angular tilting mirror (scanner II) as soon as the two scanning lenses are part of the beam path, cf. Fig. 1(e). These lenses are present to ensure that the visible laser beam enters the objective in its center, and the angle between the beam and the microscope axis creates the beam displacement on the sample surface. The scanning option based on scanner II is of especially high importance for 2LRT measurements. Such measurements can be best described by the following four measurements steps that form the basis for Secs. III–VI:

map scan can be used to free the heated map scans from any Raman mode shifts and mode broadenings induced by, e.g., strain or varying defect concentrations as further explained in Sec. VI. Finally, 2LRT map scans comprising Raman mode shifts or Raman mode broadenings can be translated into two-dimensional temperature maps based on a particular temperature calibration, cf. S-Sec. III. These temperature maps will then serve as the basis for the extraction of key parameters such as the thermal conductivity κ .

We point out that when performing PL spectroscopy and Raman thermometry (1LRT, 2LRT₀, and 2LRT) we exclusively probe steady-state conditions. Only the determination of the internal quantum efficiency η_{IQE} of the photonic membrane is based on time-resolved PL measurements issued from Ref. [46] as described in Sec. V A 2. Any temperature gradient that develops in our photonic membrane upon heating with a cw heating laser can be considered as constant over time. All experimental times like the integration time of a Raman spectrum, the step time between different positions of a 2LRT map scan, or the time until the first 1LRT, 2LRT₀, or 2LRT spectrum is recorded, are orders of magnitude larger than the thermalization time in our photonic membrane. Please see S-Sec. I for further details.

III. CHARACTERIZATION OF THE PHOTONIC MEMBRANE BY μ PL SPECTROSCOPY AND POSITIONING OF THE HEATING LASER (STEP A)

Figure 2 shows the μ PL signal of the III-nitride epilayer ($T_{amb} = 295$ K) introduced in Fig. 1, which is required for Step A. A UV laser ($\lambda_{exc} = 266$ nm), later described as the heating laser, is scanned over a corner region of the GaN pad and a μ PL spectrum is recorded for each point, yielding polychromatic μ PL map scans as shown in Figs. 2(a) and 2(b) for the $\text{In}_x\text{Ga}_{1-x}\text{N}$ ($x = 0.15$) QW emission [band-pass centered at $E_1 = 2.75$ eV, full width at half maximum (FWHM) $\Delta E_1 = 0.25$ eV] and the GaN band-edge emission ($E_2 = 3.41$ eV, $\Delta E_1 = 0.14$ eV). Two exemplary local μ PL spectra are shown in Fig. 2(c) for the two positions 1 (supported on silicon) and 2 (freestanding) identified in Figs. 2(a) and 2(b). In addition to the two main emission features (QW and band-edge emission), the onset of GaN-related defect luminescence is visible below ≈ 2.4 eV, which is of relevance for the 2LRT measurements introduced in Sec. VI.

When comparing the intensity fluctuations from Figs. 2(a) and 2(b), it is apparent that the QW emission is less homogeneously distributed across the freestanding part of the GaN membrane compared with the GaN band-edge emission. For the QW intensity distribution, numerous so-called localization centers [60] with higher emission intensity can be observed, which often can also be correlated to emission energy shifts (not shown). Here, local QW thickness fluctuations, structural defects (e.g., local assemblies of dislocations), and interrelated indium content fluctuations can lead to carrier localization [60–63]. For instance, a QW thickness fluctuation of ± 1 monolayer can already lead to emission energy shifts of $\approx \pm 60$ –70 meV for the given indium concentration [64] at room temperature and low carrier injection conditions that

are met in Fig. 2. Clearly, such thickness, indium content, and defect concentration fluctuations naturally occur during growth of III-nitride epilayers on silicon (111), cf. Sec. II A. Details regarding these carrier localization effects that are also linked to the high luminosity of this photonic membrane, despite the apparent structural defects, can, e.g., be found in Ref. [46].

The GaN band-edge emission from Fig. 2(b) shows a comparably homogeneous intensity distribution as the GaN thickness of ≈ 200 nm does not lead to any carrier confinement that would make thickness fluctuations a pronounced source of intensity variations. At the given ambient temperature $T_{amb} = 295$ K, both excitons and band-to-band transitions already contribute to the band-edge emission of GaN as the thermal energy (≈ 26 meV) has already surpassed the binding energy of the free A-exciton and B-exciton of ≈ 23 meV [65]. Here, the map scans shown in Figs. 2(a) and 2(b) already enable a first estimation of an upper bound for the effective mean exciton and carrier diffusion length $l_{diff} \leq 250$ nm, as features with the size of individual pixels appear in the map scan. Spatially resolved cathodoluminescence (CL) map scans with higher spatial resolution recorded exactly in the corner region of the GaN membrane for low injection conditions are discussed in S-Sec. II [47]. Here, an upper bound of $l_{diff} \lesssim 115$ nm is derived, which will be of relevance for the interpretation of the thermal analyses discussed in Secs. VIII and IX.

The two local spectra 1 and 2 shown in Fig. 2(c) illustrate the difference between the supported epilayer (1) and the freestanding membrane (2). The emission intensity for these locations differs by approximately a factor of two. Since the underetching process (see Sec. II A) is selective to the AlN layer, meaning that the InGaN/GaN layer stack remains unaffected, the reduction of intensity cannot be attributed to material damage. The increase in intensity here is solely associated with the difference in refractive index contrast between AlN and silicon (111) or vacuum. In addition, this observation explains the motivation for a freestanding photonic membrane that requires most light to travel along in-plane directions for commonly applied one- [43] and two-dimensional [42] cavity designs. Less apparently, but highlighted in Fig. 2(c), the QW emission and the band-edge emission exhibit an energy shift of $\approx 10 \pm 3$ meV (QW, limited by the FWHM) and 4 ± 1 meV (band edge), when comparing positions 1 and 2. This is a sign of tensile strain in the epilayer grown on silicon (111) due to lattice mismatch [66], which is released upon formation of the photonic membrane. The strain state of our III-nitride epilayer is further quantified based on μ Raman spectroscopy in Sec. IV.

After the μ PL map scan is recorded, the UV heating laser can be positioned at any desired position. We choose the position that is indicated by the purple target in Figs. 2(a) and 2(b), while the positioning precision is given by the stepping size (here $0.5 \mu\text{m}$). Once the first of the required two lasers for 2LRT₀ and 2LRT measurements has reached its position, the power can be varied to induce heating in the sample that will be probed by the second laser. Subsequent to this, the temperature probe laser needs to be positioned (Step B) by recording an unheated, nonresonant Raman map as described in the following Sec. IV.

IV. RECORDING OF UNHEATED, NONRESONANT RAMAN MAPS AND POSITIONING OF THE PROBE LASER (STEP B)

A μ Raman map scan based on nonresonant Raman spectra ($\lambda_{\text{probe}} = 488$ nm) is shown in Fig. 3(a). Here, exactly the same corner of the GaN membrane that was already probed by μ PL is now analyzed by μ Raman spectroscopy, cf. Fig. 2. As a result, control over the spatial displacement between the laser spots of the heating and the probe laser with respect to the position of the structured GaN membrane (corner) is achieved (Step B), representing a prerequisite for the Raman thermometry presented in Secs. V and VI (Steps C and D). To form the map scan from Fig. 3(a), first, nonresonant Raman spectra are recorded with a step resolution of 650 ± 50 nm without any effect on the positioning of the disengaged heating laser that was achieved via the μ PL map scan from Fig. 2. Second, the position of the E_2^{high} Raman mode of wurtzite GaN is extracted from the entire set of nonresonant Raman spectra. Plotting these Raman mode positions over the spatial coordinates lead to Fig. 3(a). Here, again as for Figs. 2(a) and 2(b), the freestanding and supported part of the GaN pad can clearly be distinguished as growth on silicon (111) leads to the formation of tensile strain in the entire epilayer, which is responsible for the additional Raman shift.

Two local spectra were recorded to illustrate the shift, at positions 1 (supported) and 2 (freestanding) as indicated in Figs. 3(a) and 3(b). Here, in addition to a strong contribution from the silicon underneath the GaN pad, the E_2^{high} Raman mode of GaN can be seen for the freestanding and supported part of the epilayer. By fitting such spectra with a suitable model, a small mode shift of 0.8 ± 0.2 cm^{-1} can be extracted, cf. Fig. 3(b). For such fitting, we employed a Lorentzian peak with an exponential background. Such an exponential background arises from the tail of the silicon Raman mode visible in Fig. 3(b).

In general, growth of GaN on silicon (111) leads to the build-up of tensile strain in the epilayer due to lattice mismatch, which can additionally be affected by the incorporation of AlN interlayers that also allow lowering the dislocation density [66]. As such dislocations are a source of relaxation, the final tensile strain state of the epilayer is given by the balance between layer thickness and the dislocation density. Based on the bisotropic (i.e., biaxial and isotropic) phonon pressure coefficient of the E_2^{high} Raman mode (2.86 $\text{cm}^{-1}/\text{GPa}$) [67], we find a minor stress release in our epilayer upon removal of the silicon (111) substrate of $\approx 0.3 \pm 0.1$ GPa. This minor stress release maintains the overall quality of the GaN membrane as, e.g., no cracks or additional structural defects are formed upon release. However, even though the assumption of a bisotropic strain situation is questioned by the particular geometry of the GaN pad corner, the value for the stress release still holds as an approximation. Only minor strain variations that are induced by the corner geometry of the freestanding GaN membrane can be observed in Fig. 3(a). Please note that the color scale chosen in Fig. 3(a) enables direct comparison with 2LRT map scans introduced in Sec. VI.

A. Nonresonant and resonant Raman spectra of GaN

Three different nonresonant and resonant Raman spectra of bulk, c -plane GaN and the c -plane GaN membrane are shown in Fig. 3(c) on a larger energy range that covers all first order Raman modes of GaN except for the longitudinal-optical (LO) modes. For a bulk piece of c -plane GaN (bottom, black spectrum), the Raman selection rules [68] are obeyed as the E_2^{low} and E_2^{high} Raman modes dominate this spectrum (allowed modes) in the chosen nonpolarized, backscattering geometry, cf. Fig. 1(e). Thus, only minor traces of the transversal-optical (TO) Raman modes $A_1(\text{TO})$ and $E_1(\text{TO})$ can be observed on the lower-wave-number side of the E_2^{high} Raman mode in addition to a broad background that arises from a defect-related μ PL signal arising from sub-band-gap optical excitation. Analyzing the GaN membrane in position 2, i.e., in the freestanding part of the GaN epilayer, yields the blue and purple spectra shown in Fig. 3(c). In spite of the large air gap (≥ 8 μm), for the middle spectrum, the Raman signal of silicon dominates the signal, while only the E_2^{high} Raman mode of GaN remains visible as again the μ PL background signal limits the dynamic range of the entire Raman spectrum, inhibiting the visibility of the E_2^{low} Raman mode. Thus, only the E_2^{high} Raman mode remains for Raman thermometry based on nonresonant spectra. In general, this situation can be improved by using a microscope objective with a numerical aperture (NA) in excess of 0.55. However, this choice is often not compatible with 2LRT thermometry employing UV heating lasers [46]. For 2LRT measurements, a dedicated UV-VIS microscope objective is required with a sufficiently large working distance for measurements in a vacuum chamber or cryostat to exclude thermal transport by convection. Furthermore, the focal planes for the two selected wavelengths need to overlap, while providing a sufficiently low curvature for the position mapping schemes for the probe laser spot as described in Sec. II B. Consequently, all these experimental requirements hinder the utilization of microscope objectives with higher NA and consequently lower depth of field in our experimental setup.

A similar situation regarding the balance between Raman and μ PL signals occurs for the resonant Raman spectrum shown in the top of Fig. 3(c) in purple. As most of the probe light ($\lambda_{\text{probe}} = 325$ nm) is absorbed in the ≈ 250 -nm-thick membrane (light penetration depth $p_{\text{GaN}}^{325\text{nm}} = 74$ nm [69]), the Raman signal of silicon is reduced when switching from the 488 nm laser (nonresonant Raman) to the 325 nm laser (resonant Raman). Please note that every value for p_{GaN} given in this paper is based on spectroscopic ellipsometry. For this method, a suitable dispersion model is fitted to experimental data and we estimate the corresponding error of p_{GaN} in the wavelength range of interest to $\pm 5\%$. A strong luminescence background occurs, which is caused by band-to-band transitions in GaN and additional contributions belonging to the resonant Raman spectrum of GaN (e.g., LO Raman modes and multiple combinations of them). Therefore, resonant Raman spectroscopy on GaN represents a challenge, as often Raman modes are covered by undesired signal. In addition, the integration time of the resonant Raman spectrum

(purple spectrum), surpasses the integration time of its non-resonant counterpart (blue spectrum) in Fig. 3(c) by a factor of ≈ 100 . Clearly, this renders such nonresonant Raman spectra more promising for mapping applications, while making also any accidental laser heating less likely due to the high transparency of the entire GaN membrane at the laser probe wavelength used in this study, cf. Sec. II A.

V. ONE- AND TWO-LASER RAMAN THERMOMETRY (STEP C)

After full positioning control is achieved for the probe and heat laser spots with respect to the corner of the GaN membrane based on Steps A and B from Secs. III and IV, the 1LRT and 2LRT₀ measurements are performed at the same sample location. The position of the probe and heat laser spots coincides for 2LRT₀ measurements. In the spirit of a step-by-step approach, the 2LRT₀ measurements serve first as a direct comparison to the common 1LRT technique, before the introduction of spatial resolution through the 2LRT measurements presented in Sec. VI.

Generally, Raman spectra enable at least three methods to measure the required temperatures. One can either measure (i) the Raman mode shift, (ii) the Raman mode broadening, or (iii) the intensity ratio of Stokes and anti-Stokes Raman modes upon variations of the power of the heating laser. Because approach (iii) typically results in uncertainties of the measured temperature that are significantly larger compared with (i) and (ii), as described in Refs. [29,70], we discard an analysis of the Stokes and anti-Stokes intensity ratios in this work. In general, an analysis of these Stokes and anti-Stokes intensity ratios is not particularly promising to map temperatures, because we found that the required integration times exceed the integration times of the Raman spectra that exclusively focus on the Stokes side by a factor of ≈ 100 in our experimental setup around T_{amb} .

A. One-laser Raman thermometry of GaN

One-laser Raman thermometry is based on resonant Raman spectroscopy. The heating laser spot is positioned at the target position in the center of the freestanding GaN pad corner as sketched in Fig. 4(a) and the wavelength utilized for heating and temperature probing is the same ($\lambda_{\text{heat}} = \lambda_{\text{probe}} = 325$ nm). Resulting resonant Raman spectra are displayed in Fig. 4(b) for rising absorbed laser power P_{abs} . The E_2^{high} Raman mode continuously shifts and broadens towards lower wave numbers, indicating a local, laser-induced heating. The corresponding Raman mode positions and FWHM values are extracted by fitting the peaks with a Lorentzian peak over a linear background, as illustrated for three P_{abs} values in Fig. 4(b) based on overlaying the experimental result (data points) with a solid line (fitting model). Position and FWHM values related to the E_2^{high} Raman mode can then be translated into local temperatures based on an equally local temperature calibration. Details regarding this local temperature calibration are given in S-Sec. III. The resulting temperature rise (T_{rise}), either based on Raman mode position or FWHM, are plotted in Fig. 4(c). Here, the horizontal axis represents P_{abs}

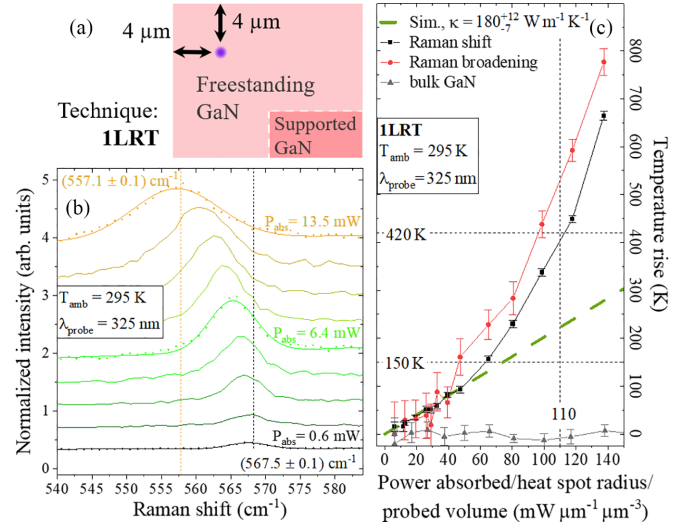


FIG. 4. (a) Scheme of the 1LRT measurements showing the position of the heating laser spot (purple) on the corner of the GaN membrane. (b) Resonant Raman spectra showing the E_2^{high} Raman mode of GaN with rising power of the heating laser ($\lambda_{\text{heat}} = \lambda_{\text{probe}} = 325$ nm) at an ambient temperature $T_{\text{amb}} = 295$ K. (c) Temperature rise induced by the heating laser plotted over its normalized absorbed power (P_{abs}). The reasoning behind this normalization of P_{abs} is given in the main text. Here, the Raman mode shift and its broadening yield different temperature rises (T_{rise}) due to the buildup of thermally induced strain in the GaN membrane. For comparison, the corresponding T_{rise} values for bulk GaN are also shown. The dashed green line illustrates our modeling for $T_{\text{rise}} \lesssim 150$ K based on a thermal conductivity $\kappa_{\text{memb}}^{\text{1LRT}} = 180_{-7}^{+12}$ W m⁻¹ K⁻¹. For more elevated powers of the heating laser, both temperature rises follow parabolas, as κ continuously decreases. The dashed horizontal and vertical lines enable the comparison to the 2LRT₀ data, cf. Fig. 5.

normalized by the product of the heat spot radius r_{abs} and the temperature probe volume to enable direct comparison to the 2LRT₀ data presented in Fig. 5 from Sec. VB, where we employ a heating laser with $\lambda_{\text{heat}} = 266$ nm. The additional normalization by r_{abs} originates from the approximation that $T_{\text{rise}} \sim P_{\text{abs}}/r_{\text{abs}}$ holds [33]. The spot sizes of the probe and heat lasers are determined via the knife-edge method (S-Sec. I A), and the probe volume is approximated by the product of the probe laser spot size and its penetration depth.

Up to $T_{\text{rise}} \approx 150$ K, the temperature rises originating from Raman mode positions and FWHM values overlap within the error bars. However, upon further increase in laser power, the FWHM of the E_2^{high} Raman mode systematically indicates higher T_{rise} values. As described by Beechem *et al.* [70], such discrepancy is caused by the buildup of thermally induced strain in the epilayer due to the local laser heating. As the heated volume tends to expand in the middle of the corner of the GaN membrane, the surrounding colder material hinders this expansion, mostly, for in-plane directions. The result is thermally induced compression in the plane of the GaN membrane around the heat spot, which is accompanied by a shift of the E_2^{high} Raman mode to higher wave numbers [67], thus, counteracting its evolution towards lower wave numbers due to laser-induced local heating. The temperature-induced

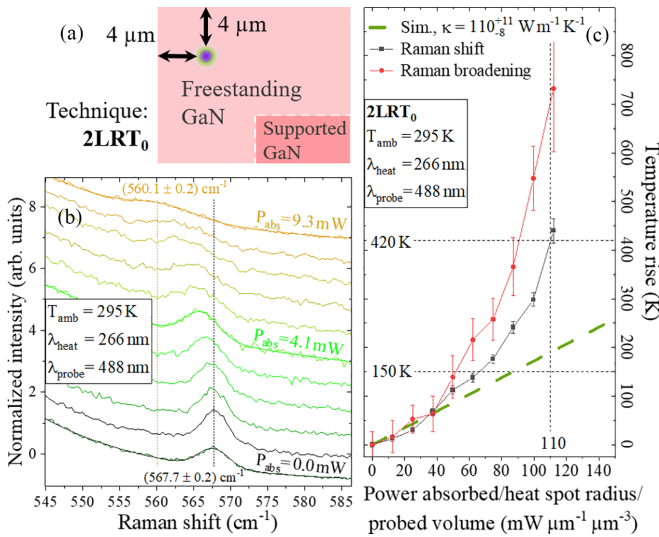


FIG. 5. (a) Scheme of the 2LRT₀ measurements without a spatial displacement between the heating laser spot (purple) and the probe laser spot (green), both positioned in the corner region of the GaN pad. (b) Nonresonant Raman spectra showing the E₂^{high} Raman mode of GaN with rising power of the heating laser ($\lambda_{\text{heat}} = 266$ nm) at an ambient temperature $T_{\text{amb}} = 295$ K. Here a probe laser wavelength $\lambda_{\text{probe}} = 488$ nm was used. (c) Temperature rise induced by the heating laser plotted over normalized absorbed laser power (P_{abs}). Here, the given normalization of P_{abs} allows direct comparison of this plot with Fig. 4(c). The Raman mode shift and its broadening yield different temperature rises due to the buildup of thermally induced strain in the GaN membrane. The dashed green line illustrates our modeling for $T_{\text{rise}} \lesssim 150$ K and a fixed thermal conductivity yielding $\kappa_{\text{memb}}^{2\text{LRT}_0} = 110_{-8}^{+11}$ W m⁻¹ K⁻¹. For more elevated powers of the heating laser, both temperature rises follow parabolas, as κ continuously decreases. The intersection of the dashed horizontal and vertical lines enable the comparison to the 1LRT data, cf. Fig. 4.

evolution of a Raman mode is not only caused by a volume effect (i.e., the thermal expansion), but also by phonon-phonon scattering events [71] that scale with the phonon population. Eventually, the Raman mode position tends to become a poor temperature sensor for $T_{\text{rise}} > 150$ K in GaN at $T_{\text{amb}} = 295$ K, while the FWHM values are not affected by thermally induced stress in a first-order approximation [67,70]. The quantification of the stress that is thermally induced by the local laser heating for $T_{\text{rise}} > 150$ K of the GaN membrane remains a task for future work.

Consequently, T_{rise} values extracted from the evolution of the FWHM values of the E₂^{high} Raman mode are best suited for determining the thermal conductivity of the GaN membrane $\kappa_{\text{memb}}^{\text{1LRT}}$. For the given normalization of P_{abs} in Fig. 4(c), the evolution of T_{rise} should follow a linear function for a fixed $\kappa_{\text{memb}}^{\text{1LRT}}$ value. However, for $T_{\text{rise}} > 150$ K the temperature trend follows a parabola, indicating a reduction of $\kappa_{\text{memb}}^{\text{1LRT}}$ with increasing T_{rise} at the given $T_{\text{amb}} = 295$ K. Commonly, it is assumed that such an evolution of $\kappa_{\text{memb}}^{\text{1LRT}}$ can be described by a power law such as $\kappa(T) = aT^{-b}$ [41] with the fitting parameters a and b . This approach has already allowed the description of the decrease of the thermal conductivity κ with increasing temperature in bulk silicon, bulk germanium [72],

and silicon membranes [41]. However, in this work, we do not focus on this particular dependence of $\kappa(T)$. The reasoning for this is mostly related to the determination of the two fitting parameters a and b . These need to be obtained from extended numerical simulations and fitting efforts beyond the scope of this work, as we do consider a more complex sample geometry, i.e., the corner of a GaN membrane and will constitute the basis of further investigations.

I. Determination of the thermal conductivity

As no straightforwardly accessible analytical solution exists for modeling the heating laser induced temperature distribution in the corner region of our GaN membrane [73], we directly turn towards finite-element simulations based on the COMSOL Multiphysics[®] software, which were already successfully applied to InP microcrystals with dimensions in the few- and submicrometer regime [30]. We operate COMSOL through scripts in MATLAB[®] using LiveLink[™]. In doing so, we enable the analysis of a large number of simulations and are able to compute errors for all κ values we derive. The procedure for extracting $\kappa_{\text{memb}}^{\text{1LRT}}$ based on the 1LRT data from Fig. 4(c) is described as follows: Details regarding the thermal model and the numerical simulations can be found in S-Sec. IV [47].

Step I. Experimental data analysis: We start by fitting a linear function to the data points from Fig. 4(c) for $T_{\text{rise}} \lesssim 150$ K. The least square regression is restricted to this range of T_{rise} values for two reasons: First, here the mode shift and the mode broadening can be applied as valid equivalent thermometers. Second, limiting the fitting to lower values of T_{rise} motivates the assumption of a constant κ_{memb} value. As a result, we obtain the slope of $T_{\text{rise}}^{\text{expt}}(P_{\text{abs}})$ in addition to the symmetric slope error.

Step II. Modeling the experiment: The numerical simulation aims to model the laser-induced heating, the thermal dissipation in the sample, and the temperature probing by a laser. To this end, the entire GaN pad along its silicon support is created inside of the simulation software with a size of 220 μm × 220 μm × 10.25 μm. The heating laser is introduced as a surfacic Gaussian heating source with an integrated power density equal to P_{abs} , while the bottom of the silicon support acts as the heat sink remaining at ambient temperature (295 K). When comparing a surfacic heating source with a volumetric heating source that considers the light penetration depth of the heating laser (p_{abs}), we found a maximal temperature deviation of less than 0.5%. For the temperature probe volume, we define a cylindrical volume over which temperatures are averaged to T_{rise} , according to Eq. (1). Here, the height of the cylinder in the cross-plane direction is given by the light penetration depth of the probe laser (p_{abs}). More details are provided in S-Sec. IV. For the case of 1LRT measurements ($\lambda_{\text{heat}} = \lambda_{\text{probe}} = 325$ nm and $p_{\text{abs}} = p_{\text{probe}} = 74$ nm) [69], the heating and probe lasers are identical, hence, they are modeled with the same parameters. For the in-plane direction T_{rise} is obtained from a Gaussian-weighted average of temperatures, considering the probe laser spot radius (r_{probe}) and its centering around the heat spot. Subsequently, the simulation is performed for all experimental P_{abs} values, yielding a linear trends for $T_{\text{rise}}^{\text{sim}}(P_{\text{abs}})$.

In addition, these simulations are repeated for a suitable range of $\kappa_{\text{memb}}^{\text{ILRT}}$. The spacing between two values of $\kappa_{\text{memb}}^{\text{ILRT}}$ is mainly determined by the slope error of the linear fit function obtained in Step I.

Step III. Deducing the thermal conductivity: We deduce $\kappa_{\text{memb}}^{\text{ILRT}}$ by comparing the slopes of the simulated and measured trends for $T_{\text{rise}}(P_{\text{abs}})$. Once the best matching simulation is found, the error of $\kappa_{\text{memb}}^{\text{ILRT}}$ is determined via the experimental slope error obtained under Step I. For a given slope and slope error of $T_{\text{rise}}^{\text{expt}}(P_{\text{abs}})$, one obtains the lower bound ($\kappa_{\text{memb}}^{\text{ILRT}} - \Delta\kappa_1$) and the upper bound ($\kappa_{\text{memb}}^{\text{ILRT}} + \Delta\kappa_2$) of the thermal conductivity with $\Delta\kappa_1 \neq \Delta\kappa_2$. Hence, we adopt the following notation for asymmetric errors: $\kappa_{-\Delta\kappa_1}^{+\Delta\kappa_2}$ [74]. These asymmetries on the error intervals can be understood based on the standard analytical relation for bulk material that relates T_{rise} to the inverse of $\kappa_{\text{bulk}}^{\text{ILRT}}$ as follows: $T_{\text{rise}}/P_{\text{abs}} \propto 1/(r\kappa_{\text{bulk}}^{\text{ILRT}})$. Here, the precise prefactor to get the equality depends on the experimental conditions as described by Lax [33].

As a result of our modeling procedure based on Steps I–III, we derive $\kappa_{\text{memb}}^{\text{ILRT}} = 180_{-7}^{+12} \text{ W m}^{-1} \text{ K}^{-1}$, illustrated by the linear function (dashed, green) shown in Fig. 4(c). This value of $\kappa_{\text{memb}}^{\text{ILRT}}$ that we extracted here for our thin photonic membrane, comprising around 200 nm of GaN and a 50-nm-thick AlN interlayer, is highly doubtful. Only GaN samples of very high crystalline quality (low structural and point defect concentrations) with a thickness of several micrometers grown on bulk GaN substrates reach such high κ values [75]. A careful analysis regarding the reliability of $\kappa_{\text{memb}}^{\text{ILRT}}$ follows in Sec. VIII along with a comparison to the results of 2LRT₀ and 2LRT measurements. Here, we reveal a systematic problem of 1LRT measurements for the given heating and probe laser spot sizes and laser penetration depths. As a precise knowledge of P_{abs} is of high importance for all 1LRT and 2LRT measurements, the following Sec. V A 2 is dedicated to its determination. Furthermore, the case of 1LRT measurements on bulk GaN is briefly described in Sec. V A 4, before 2LRT measurements are introduced in Sec. V B, following a rigorous step-by-step approach.

In this work, we focus on the low- T_{rise} limit ($T_{\text{rise}} \lesssim 150 \text{ K}$) to approximate a constant thermal conductivity κ_{memb} for our GaN membrane, which we derive based on 1LRT and 2LRT₀, as well as 2LRT measurements. In this low- T_{rise} limit, the temperature rise over normalized power of the heating laser can be approximated by a linear function, which is a first-order approximation in the spirit of a Taylor expansion that is also in use for Fig. 5(c), summarizing 2LRT₀ measurements. Higher-order terms cannot be resolved for $T_{\text{rise}} \lesssim 150 \text{ K}$, due to the limited temperature resolution of our experimental setup, cf. S-Secs. I and III. This limit for the temperature resolution predominantly originates from the optical resolution and spectral stability of our experimental setup, the temperature calibration (see S-Secs. I and III), and fitting errors [compare data and fit model in, e.g., Fig. 4(b)]. The latter errors are often connected to noise in the Raman spectra, but also additional spectral features caused by spurious PL or Raman signal. Such spurious Raman signal is, e.g., given by the Raman mode of silicon visible in Fig. 3(b) (blue Raman spectrum). Nevertheless, the comparison of the three values for κ_{memb} derived from 1LRT, 2LRT₀, and 2LRT measurements for $T_{\text{rise}} \lesssim 150 \text{ K}$

already bears interesting physical insights, as described in Sec. VIII.

2. Determination of the absorbed and the heating power

Determining a robust value for the power absorbed by the layer P_{abs} and its fraction that goes into heating P_{heat} is of high relevance for the Raman thermometry presented in this work. Generally, for the acquisition of Raman spectra, we measure the power of the heating laser between the two scanning lenses illustrated in Fig. 1(e). This position for the power measurements proved most convenient during the operation of the experimental setup. However, the power of the heating laser that reaches the surfaces of our GaN pad can only be derived based on a precise knowledge of all losses introduced by the optical elements in the beam path (lenses, mirrors, microscope objective, cryostat window). Additionally, the power of the heating laser that is reflected from the surface of the photonic membrane is determined to provide the power of the heating laser entering into the sample. In our experimental setup, the power of the reflected heating laser P_{refl} can directly be measured for every step in power of the heating laser. We then cross-checked this method by both direct, angular-dependent reflection measurements at $\lambda_{\text{heat}} = 325 \text{ nm}$ and 266 nm in a dedicated and calibrated UV-VIS spectrophotometer and by straightforward calculations based on Fresnel equations. Consequently, our direct *in situ* reflection measurements that yield P_{refl} are enabled by the specular reflection of the heating laser from the sample surface with a negligible fraction of diffusely scattered light. The high structural quality of our monocrystalline photonic membrane, as, e.g., evidenced by its structural defect density and low surface roughness (front- and backside) as detailed in Sec. II A, strongly attenuates diffuse elastic light scattering.

Furthermore, even for elevated excitation powers of the heating laser, we never observed any significant thermally induced change in reflectivity. Any reflectivity changes we measured were always directly linked to surface damage of the GaN material that only occurred at excitation powers beyond the values presented in this work. Any power that is attributed to elastic (Rayleigh scattering) and inelastic (Brillouin and Raman scattering) light scattering P_{scat} is neglected in this work as in previous works on 2LRT [39,41]. Commonly, inelastic scattering is orders of magnitude weaker than elastic scattering, while the latter is strongly reduced in our sample due to its monocrystallinity.

After the determination of the power entering the GaN pad, its transmitted fraction must be estimated to find the absorbed laser power P_{abs} . For the sake of simplicity, we treat the GaN/InGaN/GaN membrane as one effective GaN membrane with a thickness of 203 nm (3-nm-thick InGaN QW). At such GaN layer thicknesses, only 0.5% (325 nm) or 0.3% (266 nm) of the light of the heating laser are transmitted through the membrane. Thus, even though the backside of our sample is not experimentally accessible as in measurements on silicon membranes [39], we can safely assume that the power of the heating laser that enters the sample is also fully absorbed, enabling the direct determination of P_{abs} .

Furthermore, note that the absorption of GaN at 325 or 266 nm is so high [76] that Fabry-Perot interference effects

can be neglected for our GaN membrane despite its sub-wavelength thickness. In contrast, for 1LRT measurements on silicon membranes such interference effects can complicate the calculation of the absorbed power, rendering direct transmission measurements at the wavelength of the heating laser of high importance [77]. This is also especially relevant for 2LRT measurements on silicon membranes that use visible lasers for the heating (405 nm) and the temperature probing (488 nm), as demonstrated in Ref. [39]. At such wavelength in the visible spectral range, the absorption of silicon does not suffice to suppress light propagation for in-plane directions in silicon membranes. Depending on the thickness of such silicon membranes, Fabry-Perot interference effects can occur that strongly alter the overall membrane transmission. Such silicon membranes therefore require precise transmission measurements when heated with visible lasers, which in turn requires full optical access from the front- and backside of the membrane. Alternatively, a suitable modeling can be applied [77], however, this approach requires precise knowledge about the top and bottom surface roughnesses. The last step is to determine which fraction of P_{abs} leads to a local heating of the GaN membrane. In principle, one can assume that a certain fraction of P_{abs} leads to the formation of, e.g., excitons and/or electron-hole pairs, which in turn can emit light with a radiated power P_{rad} . Clearly, such light emission is one of the main aims of a photonic membrane comprising a QW as built-in light source. In the best-case scenario, the external quantum efficiency η_{EQE} of the GaN membrane would be available to evaluate the following equality: $P_{\text{abs}} = P_{\text{heat}} + P_{\text{rad}}$, with P_{heat} being the fraction of the absorbed power that went into heating.

In a light-emitting diode, η_{EQE} is defined by the number of photons emitted to free space per second divided by the number of injected electrons per second. However, despite the numerous μPL results shown in Fig. 2, η_{EQE} of the present sample is low at $T_{\text{amb}} = 295\text{K}$. In Ref. [46] time-resolved PL measurements were performed between 5 and 295 K to measure the internal quantum efficiency η_{IQE} of exactly the GaN membrane structure used for the present work. Here η_{IQE} is again defined in a light-emitting diode by the number of photons emitted from the active region per second divided by the number of injected electrons per second. Consequently, the time-resolved PL analysis yielded $\eta_{\text{EQE}} < \eta_{\text{IQE}} \approx 0.1\%$ for $T_{\text{amb}} = 295\text{K}$. Thus, we can safely assume $P_{\text{abs}} \approx P_{\text{heat}}$ for the present sample at room temperature and beyond. However, this situation would change if the sample was cooled towards, e.g., 5 K or if in general a sample with less nonradiative defects would be analyzed, which remains a task for future work. Adding an InGaN underlayer to our structure grown on silicon as described by Haller *et al.* would already drastically boost η_{IQE} at room temperature [58]. Nevertheless, already the present sample's PL signal rises by up to four orders of magnitude when transitioning from 295 to 5 K, which is accompanied by η_{IQE} reaching several tens of percent at 5 K.

3. Experimental determination of the temperature

The temperature derived from our experiments is either based on the Raman mode shift or broadening, which are in turn acquired from every point under the laser spot. Strictly

speaking, the technique does not probe the local temperature but its average under the laser spot, weighted by the beam profile intensity and its penetration depth [29,78]:

$$T_{\text{meas}} = \int_V drd\theta dz r T(r, \theta, z) f_{\text{probe}}(r, \theta, z) \quad (1)$$

with $f_{\text{probe}}(r, \theta, z)$ being the weighting function of the probe laser and $T(r, \theta, z)$ the local temperature of the sample. The weight function $f_{\text{probe}}(r, \theta, z)$ can be written as product of the probe laser beam profile (assumed to be a Gaussian) and the attenuation of the backscattered probe laser beam:

$$f_{\text{probe}}(r, \theta, z) = \frac{1}{w_e \sqrt{\pi}} \exp\left(-\frac{(r-r_0)^2}{w_e^2}\right) \exp\left(-\frac{2z}{p_{\text{probe}}}\right), \quad (2)$$

with w_e being the beam waist as the beam intensity is reduced to $1/e$ of its initial value, r_0 the location of the probe beam, p_{probe} the penetration depth of the laser, and r , θ , and z a cylindrical coordinate system centered at the probe beam spot location. The factor of two in the attenuation term accounts for the probe beam travel to depth z into the material and its return to the material surface. To extract the coefficient of thermal conductivity κ , we compare T_{meas} to numerical simulations. As the outcome of such simulations is usually the simulated local temperature $T_{\text{sim}}(r, \theta, z)$, it needs to be averaged by a function that models the probe laser:

$$f_{\text{probe}}^{\text{sim}}(r_{\text{sim}}, \theta_{\text{sim}}, z_{\text{sim}}) = \frac{1}{w_e \sqrt{\pi}} \exp\left(-\frac{(r_{\text{sim}}-r_0)^2}{w_e^2}\right) \exp\left(-\frac{2z_{\text{sim}}}{p_{\text{probe}}}\right), \quad (3)$$

with r_{sim} , θ_{sim} , and z_{sim} being the cylindrical *simulated* coordinates, to distinguish from the physical ones. w_e and r_0 are measured and inserted in the model and p_{probe} comes from Ref. [69].

4. One-laser Raman thermometry on bulk GaN

1LRT measurements are frequently reported in literature and were, e.g., applied to bulk germanium [30], bulk silicon [79], and related membranes [77]. However, performing such measurements on bulk GaN already represents a challenge for the reasons given in Sec. IV A. Nevertheless, we recorded the required resonant Raman spectra of bulk GaN with $\lambda_{\text{heat}} = \lambda_{\text{probe}} = 325\text{nm}$, showing the E_2^{high} Raman mode of GaN, cf. S-Sec. IV [47]. Even when raising the laser power to the maximum laser power available, no Raman mode shift or Raman mode broadening as a sign of local heating occurred. The corresponding temperatures are shown for bulk GaN in Fig. 4(c). Thus, the thermal conductivity of high quality bulk GaN κ_{bulk} cannot be measured by 1LRT in our setup as described in S-Sec. IV. Even a further increase of the power of the heating laser does not represent a promising pathway for 1LRT measurements on bulk GaN with very high thermal conductivities, as also any heating laser-induced material damage must always be avoided.

B. Two-laser Raman thermometry of GaN

The results of 2LRT₀ measurements without a spatial displacement are shown in Fig. 5. Again the heating laser (purple, $\lambda_{\text{heat}} = 266$ nm) is positioned at the same position as for the 1LRT measurements, cf. Fig. 4(a). However, now this heating laser is superimposed with the probe laser (green, $\lambda_{\text{probe}} = 488$ nm) as sketched in Fig. 5(a). Upon varying the power of the heating laser, nonresonant Raman spectra are recorded with the probe laser and are shown for the wave number range around the E_2^{high} Raman mode in Fig. 5(b). Again a suitable fitting model is applied to the Raman spectra to extract the position and FWHM of the E_2^{high} Raman mode of GaN with rising power of the heating laser. A Lorentz peak with an exponential background is best suited for fitting the E_2^{high} Raman mode in close energetic vicinity of the omnipresent Raman mode of silicon. Resulting fitting functions are illustrated in Fig. 5(b) for selected powers of the heating laser.

Interestingly, it is mainly the Raman mode of silicon that proves to be a hurdle for the accurate determination of the Raman mode position and broadening at elevated powers of the heating laser. As a result, the corresponding error bars get larger at high powers, as shown in Fig. 5(c). However, this is not a general limitation of 2LRT₀ measurements but rather a specificity of the photonic membrane supported by silicon. As 2LRT₀ measurements are always conducted for identical powers of the probe laser, a solid determination of elevated temperatures can in principal be achieved. In contrast, the 1LRT measurements summarized in Fig. 4(c) prove in general challenging for low powers of the heating laser due to the resulting low Raman signal that serves as temperature probe.

From the Raman mode positions and FWHM values, two local temperatures can be extracted based on our local temperature calibration, cf. S-Sec. III [47]. Similar to the results of the 1LRT measurements, the two trends for the local temperatures shown in Fig. 5(c) start to deviate from each other at a T_{rise} value of about 150 K. Our subsequent method to extract the thermal conductivity from our 2LRT₀ measurements $\kappa_{\text{memb}}^{2\text{LRT}_0}$ is similar to our evaluation of the 1LRT measurements described in Sec. V A based on Steps I–III. The only major difference is now related to the heat and probe volume due to the different wavelengths of the heating and probe lasers. As the GaN membrane is transparent to the probe laser, the corresponding temperature probe volume for our simulations now corresponds to a cylinder with a height of 203 nm and a radius of 600 nm, which includes the QW for the sake of simplicity. See S-Sec. IV for details regarding the modeling.

For $T_{\text{rise}} \lesssim 150$ K we derive $\kappa_{\text{memb}}^{2\text{LRT}_0} = 110_{-8}^{+11}$ W m⁻¹ K⁻¹ as illustrated by the linear function (dashed, green) illustrated in Fig. 5(c). Again, here the sub- and superscript of this value denote the lower and upper bound of the asymmetric error interval. The reliability of this value for $\kappa_{\text{memb}}^{2\text{LRT}_0}$ and its obvious discrepancy to the higher value of $\kappa_{\text{memb}}^{1\text{LRT}} = 180_{-7}^{+12}$ W m⁻¹ K⁻¹ will be discussed in Sec. VIII. As the increase in the temperature probe volume will be key to an understanding of $\kappa_{\text{memb}}^{2\text{LRT}_0} < \kappa_{\text{memb}}^{1\text{LRT}}$, it is promising to further increase the temperature probe volume by scanning the probe laser across the focus of the heating laser during 2LRT measurements as described in the following Sec. VI.

Please note that the slope of the green dashed line (simulated T_{rise} values for a fixed κ) in Fig. 4(c) is steeper than its equivalent in Fig. 5(c). This could appear counterintuitive as in general one expects higher values of the thermal conductivity κ to result in smaller temperature rises. However, the slope additionally depends on the heat laser spot radius and the temperature probe volume. The heat laser spot radius equals 600 nm for the 1LRT measurements from Fig. 4(c), which surpasses the corresponding value for the 2LRT₀ measurements (250 nm), hence explaining the aforementioned slope discrepancy. See Sec. V A for details regarding the normalization of the x axis in Figs. 4(c) and 5(c).

VI. SPATIALLY RESOLVED TWO-LASER RAMAN THERMOMETRY (STEP D)

To derive spatially resolved temperature map scans by 2LRT measurements, it is necessary to displace the probe laser ($\lambda_{\text{probe}} = 488$ nm) from the heating laser ($\lambda_{\text{heat}} = 266$ nm). One then obtains Raman map scans showing, e.g., the position of the E_2^{high} Raman mode extracted from nonresonant Raman spectra, depending on the spatial coordinates as shown in Fig. 6(a). Here, the position of the focus spot of the heating laser is clearly visible close to the corner of the membrane, as locally an additional Raman mode shift towards lower wave numbers is induced. This additional Raman mode shift was missing in the unheated Raman map scan from Fig. 3(a). By subtracting the locally heated Raman map scan in Fig. 6(a) from this unheated Raman map scan in Fig. 3(a), one can now determine the spatial distribution of the Raman mode shift that is exclusively induced by the local heating. By applying a suitable local temperature calibration (see S-Sec. III), we can translate these Raman mode shifts to temperatures as shown in Fig. 6(b). Strain variations that induced Raman mode shifts in the not locally heated Raman map scan are eliminated by this approach. This is observable in Fig. 6(a), when looking at the area enclosed by a black dashed line. Here, the area of fully supported GaN is visible due to the occurrence of tensile strain. Exactly this area is no longer visible in the temperature map scan of Fig. 6(b) due to the subtraction of map scans. Please note that the zigzag shape of the upper edge of the corner shown in this temperature map is exclusively caused by the step resolution in our Raman map scans of ≈ 650 nm. From a temperature map scan as shown in Fig. 6(b), one can now extract temperature profiles for any in-plane direction. Corresponding temperature profiles are shown in Fig. 6(c) for the a and m directions in the c plane of the GaN membrane. Exactly such cut lines through a temperature map scan resulting from 2LRT measurements can form the basis for extracting the thermal conductivity for all in-plane directions.

In Fig. 7 we exemplify the determination of the thermal conductivity $\kappa_{\text{memb}}^{2\text{LRT}}$ based on 2LRT measurements. Therefore, Fig. 7(a) shows the spatial evolution of temperatures extracted from the shift of the E_2^{high} Raman mode for $P_{\text{abs}} = 4.0$ mW. The data shown match the experimental data depicted in Fig. 6(c) for the m direction in our c -plane GaN membrane. First, we obtain a linear least square fit (dashed black line) to the experimental temperature values (black circles), which are plotted over logarithmic distances u to the heat spot in

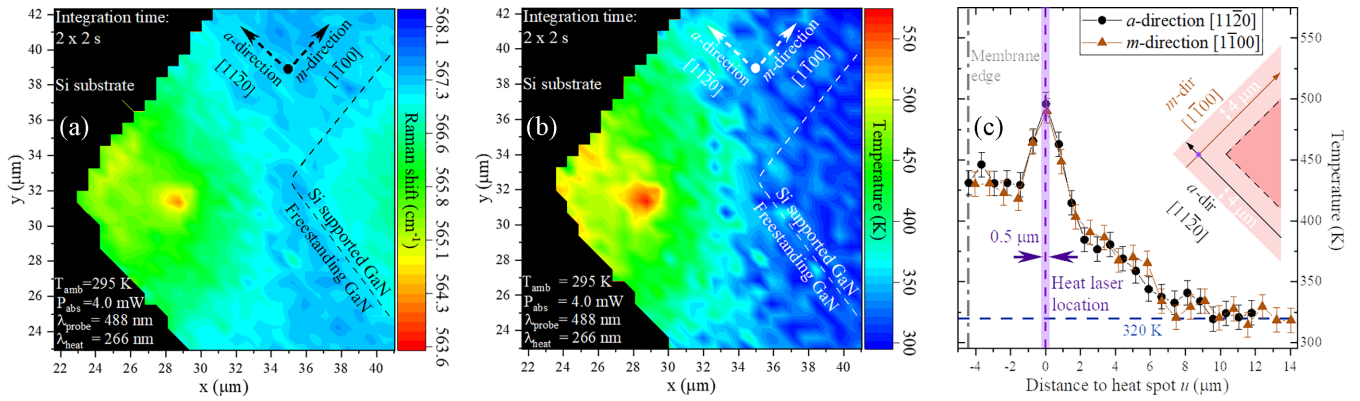


FIG. 6. (a) Raman map illustrating the position of the E_2^{high} Raman mode extracted from nonresonant Raman spectra ($\lambda_{\text{probe}} = 488 \text{ nm}$) at an ambient temperature of 295 K. The effect of the simultaneously engaged heating laser ($\lambda_{\text{probe}} = 266 \text{ nm}$) can directly be observed close to the corner of the GaN membrane. There, an additional Raman mode shift can be seen, which is induced by the heating laser. See Fig. 3(a) for the same, but nonlocally heated Raman map. (b) By subtracting the unheated Raman map from the locally heated map, one can derive a temperature map based on a suitable calibration (see main text). (c) Cut lines showing the evolution of the temperature rise along the a (circles) and m direction (triangles) in the c plane of the GaN membrane. Here, the sample edge as well as the location and spot size of the heating laser are illustrated.

Fig. 7(a). Here a linear fit to the experimental data is adequate due to the analytical solution of the Fourier equation for an infinite two-dimensional membrane [39]. In addition, we also obtained corresponding 1σ and 2σ confidence intervals for the slopes from the linear least square fit, which are illustrated as gray-shaded areas in Fig. 7(a). Note that the intercept in the fit is not considered for the analysis.

Subsequently, we fit our already spatially resolved thermal model described in Sec. V A 1 and S-Sec. IV to the experimental temperatures by scanning through a range of $\kappa_{\text{memb}}^{2\text{LRT}}$ values in steps of $5 \text{ W m}^{-1} \text{ K}^{-1}$. This stepping matches half of the error of the final value of $\kappa_{\text{memb}}^{2\text{LRT}}$, aiming to avoid the introduction of uncertainties from the data analysis. In Fig. 7(a) we illustrate this procedure by showing the simulated temperature trends for different $\kappa_{\text{memb}}^{2\text{LRT}}$ values ranging from 20 to $165 \text{ W m}^{-1} \text{ K}^{-1}$ in steps of $15\text{--}20 \text{ W m}^{-1} \text{ K}^{-1}$ by the solid, color-coded lines.

To determine the error of the $\kappa_{\text{memb}}^{2\text{LRT}}$ value that reaches the best agreement with the experimental data, we match the slopes of the numerical temperature trend to the boundaries of the 2σ confidence interval shown in Fig. 7(a). As a result, we obtain asymmetric error bars for $\kappa_{\text{memb}}^{2\text{LRT}}$ by our numerical fitting model similar to the error bars belonging to $\kappa_{\text{memb}}^{2\text{LRT}_0}$ and $\kappa_{\text{memb}}^{1\text{LRT}}$, cf. Sec. V. This approach resembles the fitting procedure described in Sec. V under Step III. As a result, for the experimental temperature values that were extracted from Raman mode shifts, we obtain $\kappa_{\text{memb}}^{2\text{LRT}} = 95_{-7}^{+11} \text{ W m}^{-1} \text{ K}^{-1}$ based on our numerical fitting approach. Please note that we restrict our numerical fitting approach to $T_{\text{rise}} \lesssim 150 \text{ K}$ to avoid a thermally induced lowering of $\kappa_{\text{memb}}^{2\text{LRT}}$, similar to the data analysis of the 1LRT and 2LRT₀ measurements presented in Sec. V.

Similar experimental data along with the corresponding modeling is shown in Fig. 7(b) for temperature values extracted from the broadening of the E_2^{high} Raman mode with temperature. However, for the given $P_{\text{abs}} = 4.0 \text{ mW}$ value, we observe a large scatter of the temperature values in Fig. 7(b)

and consequently in the thermal conductivities presented in Fig. 8. That is because the determination of the mode width by fitting relies on finding the maximum of the peak and its baseline. Each of these steps introduces errors that rely on the signal-to-noise ratio of the Raman signal, while temperatures obtained from the Raman mode shift only rely on finding the maximum of the peak, cf. Fig. 7(a). Thus, the numerical fitting of cut lines extracted from the mode broadening [Fig. 7(b)], leads to an uncertainty on the thermal conductivity so large that within the standard 2σ confidence interval, the T vs $\ln(u)$ slope can be equal to zero. This results in an upper bound for the thermal conductivity of $+\infty$, cf. Fig. 8.

In Fig. 8 we summarize all our $\kappa_{\text{memb}}^{2\text{LRT}}$ values for three different values of P_{abs} and the two selected crystal directions in the c plane of our GaN membrane. Here, we also state the maximal value of T_{rise} among the range of the experimental temperatures that were fitted by our numerical approach. As Fig. 8 shows, values for $\kappa_{\text{memb}}^{2\text{LRT}}$ that are based on the Raman mode broadening (red symbols) show significantly larger error bars compared with their counterparts arising from the Raman mode shift (black symbols). For this reason for $P_{\text{abs}} = 2 \text{ mW}$ we can only obtain meaningful values for $\kappa_{\text{memb}}^{2\text{LRT}}$ based on the mode shift. Interestingly, all $\kappa_{\text{memb}}^{2\text{LRT}}$ values that originate from Raman mode shifts in Fig. 8 indicate thermal conductivities around $95_{-7}^{+11} \text{ W m}^{-1} \text{ K}^{-1}$. In contrast, while for $P_{\text{abs}} = 4.0 \text{ mW}$ the $\kappa_{\text{memb}}^{2\text{LRT}}$ values originating from Raman mode broadenings still overlap with their counterparts originating from Raman mode shifts, an increasing deviation can tentatively be observed towards $P_{\text{abs}} = 6.7 \text{ mW}$. This is connected to the corresponding T_{rise} values at our highest heating power, which yield $T_{\text{rise}} \leq 170 \text{ K}$ for the Raman mode shift (black symbol) and $T_{\text{rise}} \leq 300 \text{ K}$ for the Raman mode broadening. For the latter case, such drastic increase in temperature yields a decline of the measured $\kappa_{\text{memb}}^{2\text{LRT}}$ value, which matches our observation from Figs. 4 and 5, where we observed a parabolic evolution of T_{rise} with increasing power of

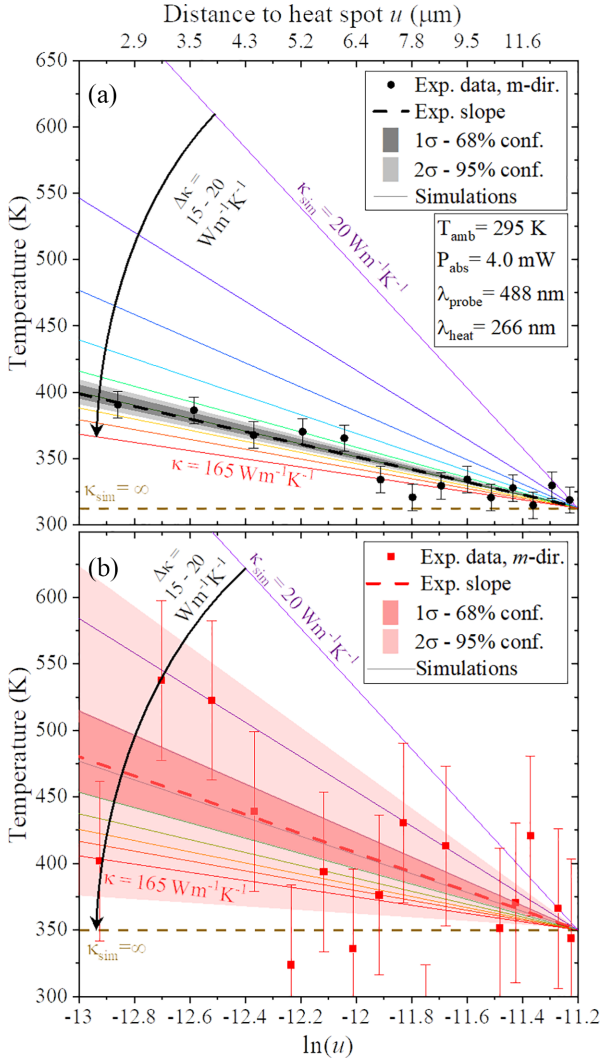


FIG. 7. (a) Temperature profile plotted over the logarithmic distance to the center of the heat spot u (black circles). These experimental data match the temperature data relying on the Raman mode shifts introduced in Fig. 6(c) for the m direction. A linear least square fit to the data is shown by the dashed, black line, while the corresponding 1σ and 2σ confidence intervals are also shown. The solid, color-coded lines show a subset of the simulated temperature trends for different $\kappa_{\text{memb}}^{2\text{LRT}}$ values ranging from 20–165 $\text{W m}^{-1} \text{K}^{-1}$ in steps of 15–20 $\text{W m}^{-1} \text{K}^{-1}$. We do not show the full set of simulated curves, in steps of 5 $\text{W m}^{-1} \text{K}^{-1}$, to lighten the image. Here, the horizontal dashed line illustrates an infinite thermal conductivity. (b) Similar data for the temperature profile extracted from the Raman mode shift broadening. Here, a much larger fluctuation is visible for the experimental data (red rectangles), which challenges any meaningful determination of $\kappa_{\text{memb}}^{2\text{LRT}}$ at the given value of $P_{\text{abs}} = 4.0$ mW.

the heating laser for the same reason. Furthermore, within the given error bars, no directional anisotropy can be determined for $\kappa_{\text{memb}}^{2\text{LRT}}$ in the c plane of our GaN membrane.

VII. AB INITIO COMPUTATION OF PHONON TRANSPORT

To theoretically compute the thermal conductivity κ , we use an *ab initio* solution of the linearized phonon Boltzmann

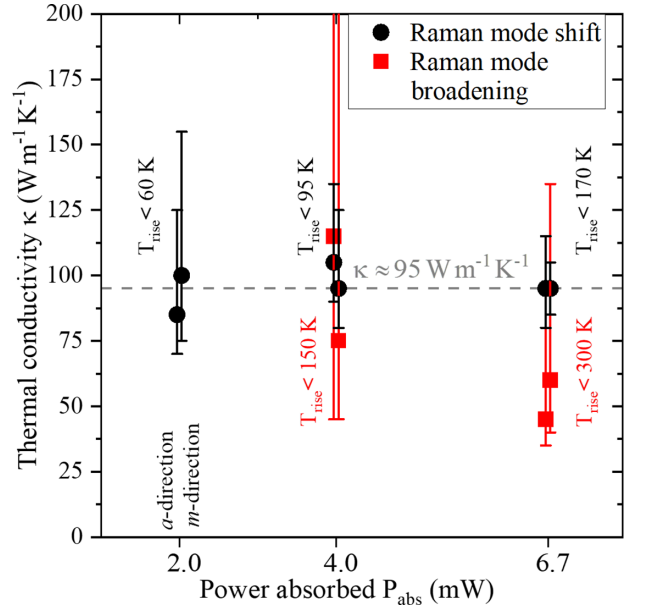


FIG. 8. Summary of all $\kappa_{\text{memb}}^{2\text{LRT}}$ values found for different values of P_{abs} based on 2LRT measurements either relying on Raman mode shifts (black circles) or Raman mode broadenings (red squares). Here, the a and m direction in the c plane of our photonic membrane are considered, as illustrated in the inset of Fig. 6(c). In addition, the upper bound for the T_{rise} interval is given, which formed the basis for the extraction of $\kappa_{\text{memb}}^{2\text{LRT}}$. Comparably large error bars for the $\kappa_{\text{memb}}^{2\text{LRT}}$ values based on Raman mode broadening (red symbols) originate from the large scatter among the spatially resolved temperatures as shown in Fig. 7(b). This scatter is so large that it made it impossible to extract a meaningful thermal conductivity when $P_{\text{abs}} = 2.0$ mW, as the maximal T_{rise} observed was almost completely within the noise level. Finally, we determine $\kappa_{\text{memb}}^{2\text{LRT}} = 95_{-7}^{+11}$ $\text{W m}^{-1} \text{K}^{-1}$ from our experimental temperature trends solely based on the Raman mode shift.

transport equation (BTE), which furnishes the mode (branch s , wave vector \mathbf{q}) resolved steady-state distribution function

$$n_{\text{sq}} = n_{\text{sq}}^0 \left[1 - (1 + n_{\text{sq}}^0) \frac{\nabla T \cdot \mathbf{F}_{\text{sq}}}{k_B T} \right], \quad (4)$$

where n^0 is the equilibrium Bose-Einstein distribution, T is the crystal temperature, ∇T is the applied temperature gradient, k_B is the Boltzmann constant, and $k_B^{-1} \mathbf{F}_{\text{sq}}$ is a vectorial “mean free displacement” [80] carrying the units of length. This quantity is essentially a measure of how far each phonon mode is moved out of equilibrium due to the presence of the temperature gradient field.

The phonon BTE can be conveniently cast in the following form:

$$\mathbf{F}_{\text{sq}} = \mathbf{F}_{\text{sq}}^0 + \Delta \mathbf{F}_{\text{sq}}^S[\mathbf{F}], \quad (5)$$

where the first term on the right-hand side is the mode-resolved relaxation-time approximation (RTA) expression and the second, nonlocal term gives the in-scattering corrections. The expressions for these terms have been given before in, e.g., Ref. [81]. A full self-consistent solution of this equation takes us beyond the RTA.

From the solution of the BTE, a scalar, phonon mean-free path (MFP) is constructed in the following manner:

$$l_{\text{sq}}^{\text{MFP}} = \frac{\mathbf{F}_{\text{sq}} \cdot \mathbf{v}_{\text{sq}}}{k_{\text{B}} v_{\text{sq}}}, \quad (6)$$

where \mathbf{v} is the phonon group velocity.

The phonon thermal conductivity tensor is given by

$$\kappa = \frac{1}{V k_{\text{B}} T} \sum_{\text{sq}} \hbar \omega_{\text{sq}} n_{\text{sq}}^0 (1 + n_{\text{sq}}^0) \mathbf{v}_{\text{sq}} \otimes \mathbf{F}_{\text{sq}}, \quad (7)$$

where \hbar is the reduced Planck constant, ω is the phonon angular frequency, and V is the crystal volume.

In wurtzite crystals, the thermal conductivity has the following structure: $\kappa_{xx} = \kappa_{yy} \neq \kappa_{zz}$, with the off-diagonal terms identically zero. In the harmonic approximation, phonons are infinitely long-lived collective excitations of the crystal. Anharmonicity is captured via the quantum-mechanical interactions between the phonons (ph). In this work, we included 3ph and 4ph interactions. We have also included the ph-(iso)tope scattering within the Tamura model [82]. Phonon-boundary scattering, hereafter referred to as *ph-thin-film*, is included empirically via [83]

$$\tau_{\text{sq,ph-thin-film}}^{-1} = \frac{2v_{\text{sq}}^{\perp}}{h}, \quad (8)$$

where v^{\perp} is the phonon group-velocity component perpendicular to the plane of the film and h is the film thickness. Equation (8) includes diffuse scattering with the top and bottom facets of the GaN membrane (see Fig. 1). We note that it is possible to derive more refined expressions for boundary scattering, including in-plane [84] (commonly known as the Fuchs-Sondheimer model) and cross-plane directions [85]. The development of these models is beyond the scope of this work and will be considered in future works.

While the real-life sample contains dislocation defects and charge carriers, we have not included the effects of the presence of these in our current calculations. Each of these excluded phonon scattering channels degrades the thermal current further and, as such, the theoretical prediction made here should be interpreted as an upper limit of the actual κ . Nevertheless, our computation of κ and the l^{MFP} values will prove valuable for the qualitative comparison to the experimental results that we obtain from our different thermometric techniques, cf. Sec. VIII.

A. Computational details

We use the QUANTUM ESPRESSO suite [86–88] for our density functional theory (DFT) and density functional perturbation theory (DFPT) calculations. We employ the optimized norm-conserving Vanderbilt (ONCV) [89] pseudopotential with the local density approximation for the exchange correlation function. The relaxed lattice constants are $a = 3.15 \text{ \AA}$ and $c = 5.14 \text{ \AA}$.

The second-order force constants (2FCs) required for the harmonic properties are computed using DFPT with a $6 \times 6 \times 6$ wave-vector mesh. The third-order force constants (3FCs) needed for the three-phonon scattering are calculated using the displaced supercell method. For this, the THIRDDORDER

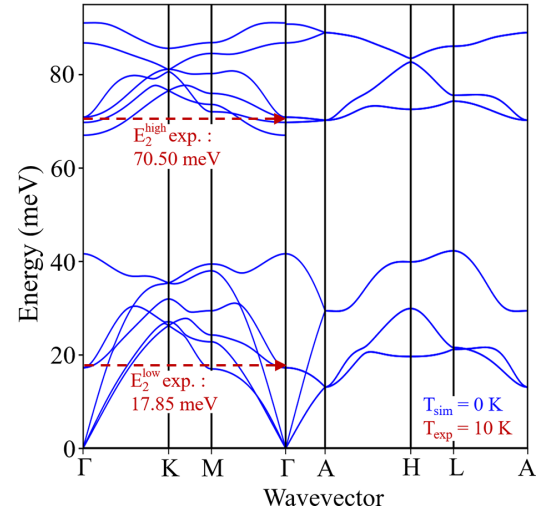


FIG. 9. Calculated phonon dispersions along high-symmetry paths in the Brillouin zone for GaN at 0 K. We observe a total of 12 branches: three acoustic+three low-lying optical phonon modes separated by an energy gap from the six high-lying optical phonon modes. The experimental energies of the E_2^{high} and E_2^{low} optical modes measured at 10 K are indicated by the red dashed arrows close to the Γ point.

code [80] is used to generate an irreducible set of $4 \times 4 \times 4$ (256 atoms) supercells with two displaced atoms. Following the self-consistent-field (SCF) DFT calculations on these supercells using a Γ -point sampling of the electronic reciprocal space, the 3FCs are read out using again the THIRDDORDER code. In this work, we include four-phonon scattering since, in general, it is not possible to know *a priori* whether this will significantly limit the phonon transport or not. To calculate the four-phonon scattering rates, we need the fourth-order force constants (4FCs). For this, we use the FOURTHORDER [90] code to generate 256-atom supercells with three atoms displaced in each. Following the SCF calculations, the same code is used to read-out the 4FCs. Furthermore, the FOURPHONON code [90] is used to generate the four-phonon scattering rates on a coarse $12 \times 12 \times 12$ phonon wave vector (\mathbf{q}) mesh, $\tau_{4\text{ph,coarse}}^{-1}$.

The 2FCs, 3FCs, and $\tau_{4\text{ph,coarse}}^{-1}$ are fed into ELPHBOLT [81] which calculates the phonon transport properties by solving the BTE on a converged $36 \times 36 \times 36$ \mathbf{q} -mesh. The code calculates harmonic properties and three-phonon scattering rates using the 2FCs and 3FCs, respectively. The energy conserving δ functions are calculated using the analytic tetrahedron method [91]. The $\tau_{4\text{ph,coarse}}^{-1}$ are calculated on the fine transport \mathbf{q} mesh using an (in general tri-) linear interpolation method. We use this indirect method for computing the 4ph scattering rates on the transport \mathbf{q} mesh since the direct computation of this quantity on such a fine mesh is prohibitively expensive at the moment. The RTA term, \mathbf{F}^0 , is constructed using Matthiessen's rule where the total scattering rate is given by $\tau_{\text{total}}^{-1} = \sum_x \tau_x^{-1}$, where $x = \{\text{ph-iso, ph-thin-film, 3ph, 4ph}\}$. In the full solution of the BTE, the in-scattering correction due to the 3ph interactions is added back iteratively. The thin-film is modeled as having a 250 nm height along the crystal c axis and an infinite extent in the c plane.

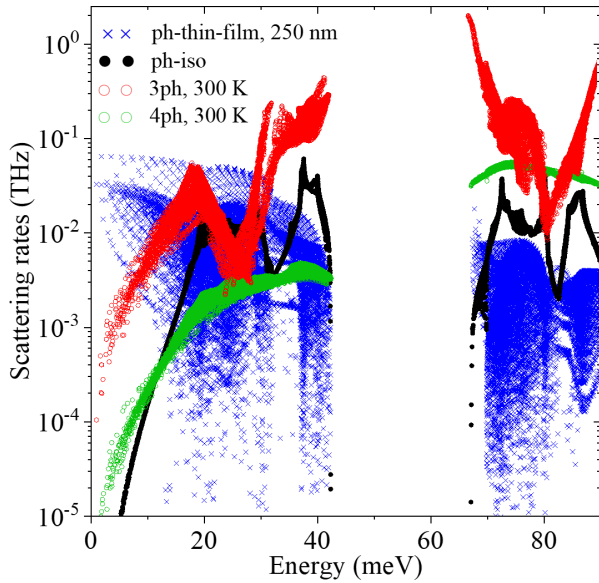


FIG. 10. Room-temperature phonon scatterings rates in the RTA for the various scattering channels included in the simulation. Because of the energy gap around 50 meV, two phonons with energies around 25 meV cannot coalesce together, creating a dip around 25 meV in the 3ph scattering channel. This dip is completely absent in the 4ph scattering process since no such restriction exists.

B. Presentation of the theoretical results

We present in Fig. 9 the calculated phonon dispersions at 0 K. The three acoustic + three low-lying optical phonon branches are separated from the six high-lying optical phonon branches by a large energy gap which, as we shall see shortly, has important consequences for the thermal transport properties of this material. The two red arrows indicate the experimental energies of the E_2^{high} and E_2^{low} optical modes, measured at 10 K, in comparison to the calculated ones.

Figure 10 shows the 300 K, RTA scattering rates of phonons due to their interactions in the various scattering channels included in the simulation. We discuss here some salient features of the acoustic scattering rates that highlight the roles of the different competing interactions. First, the 3ph scattering rates (empty red circles) show a pronounced dip in the 20–30 meV energy range. As such, the phonon-isotope scattering (black circles) becomes dominant in this energy window. The large dip can be connected to the phonon dispersions of the material. Specifically, the presence of the large gap between the acoustic + low-lying optic and the high-lying optic sectors results in a reduction in the 3ph scattering phase space, explaining the corresponding dip in the scattering rates. One can understand this by noticing in Fig. 9 that two ≈ 25 meV phonons cannot coalesce since there is no 50 meV state available in the spectrum. In contrast, three ≈ 25 meV phonons can indeed coalesce, explaining that fact that no such dip in the 4ph scattering rates (empty green circles) is present. As such, the 4ph scattering rates become important, even at 300 K. This suggests that, at higher temperatures, the 4ph interaction will play a progressively stronger role and will cause a stronger than T^{-1} scaling of κ . Observation of such a deviation from the T^{-1} scaling of κ has been reported in

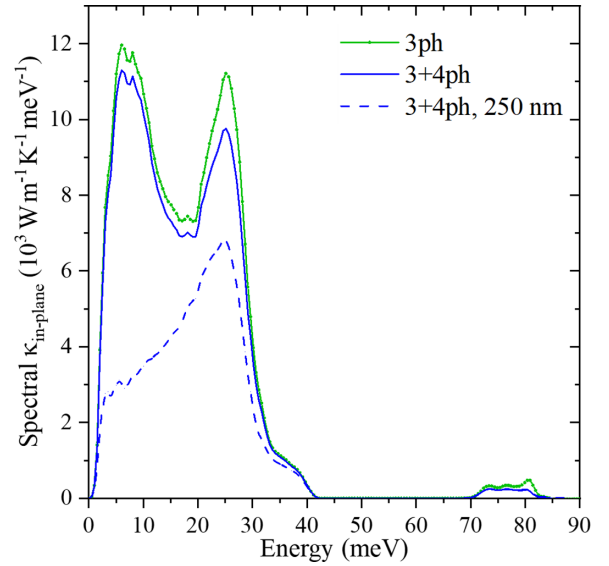


FIG. 11. Room-temperature spectrum of $\kappa_{\text{in-plane}}$ for an infinite GaN crystal and a 250-nm-thick GaN membrane. Phonon-isotope scattering is included in all three cases. Of the two peaks visible for the infinite crystal (solid green and blue line), the one corresponding to the acoustic modes is the most affected by the introduction of the top and bottom facets boundary scattering caused by our membrane (dashed blue line).

Ref. [92]. Next, we focus on the high-energy optic phonons. As for the low-energy optic phonons, because of scattering phase-space restrictions of the 3ph scattering rates, the 4ph scattering rates become important in the 70–85 meV energy range. However, these phonons do not directly transport heat since they have high scattering rates and/or have low group velocities. Lastly, The ph-thin-film scattering (blue crosses) rates are weakly dependent on energy and are high for the heat-carrying phonons. This, as we shall see below, makes them a strong limiter of the κ even at 300 K.

Next, we plot the energy spectrum of the $\kappa_{\text{in-plane}}$ in Fig. 11. The ph-iso scattering is included in all the cases presented. For the 3ph limited case (green dot-line), we see two dominant peaks in the 3–12 and 20–30 meV range. The lower energy peak is due to high-velocity acoustic phonons while the second peak is due to the dispersive low-lying optic phonons. The low-energy peak follows from the classical Slack criteria for high- κ materials [93]. The second peak, on the other hand, is enabled by the fact that the 3ph scattering rates show an anomalous dip, as explained in the previous paragraph, reminiscent of the material BAs [93]. The optic phonons across the energy gap contribute negligibly to the thermal conductivity. Next, with the 4ph scattering turned on, we see a general reduction in the κ contribution (blue curve), especially in the 20–30 meV energy range. Lastly, the thin-film scattering causes a significant reduction in the spectral κ (dashed blue line), especially for the low-energy region where this is the dominant scattering channel. The second peak is also significantly reduced, albeit to a lesser extent than the first, evidently owing to the anomalous weakening of the 3ph scattering rates. The strong suppression of the low-energy peak due to the thin-film scattering suggests that the low-energy

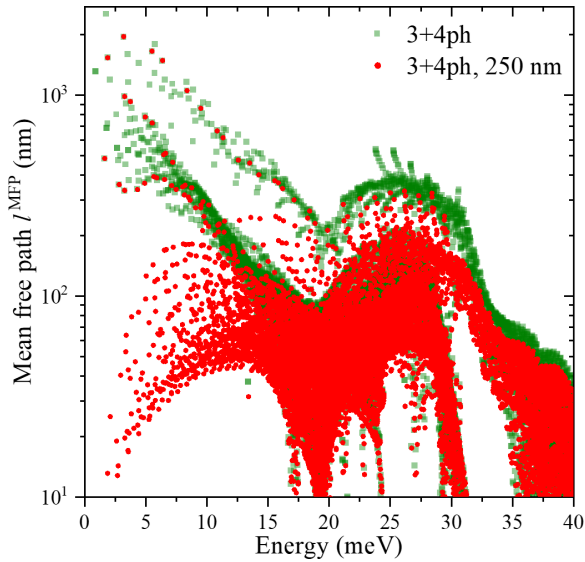


FIG. 12. Room-temperature phonon mean-free path l^{MFP} for the acoustic and low-lying optical phonons, with and without the introduction of the top and bottom facets boundary scattering. Phonon-isotope scattering is included in both cases. We observe a strong reduction of the acoustic modes' mean-free paths, due to the large cross-plane component of their velocities. Some phonons are, however, barely affected by the introduction of boundary scattering; these are phonons with a vanishing cross-plane component of their velocities.

acoustic phonons are carrying heat ballistically. In contrast, the moderate suppression of the second peak suggests diffusive transport of the phonons in that energy range since the isotope, 3ph, and 4ph, all play an important role in degrading the heat current.

The effect of the thin-film on the phonon transport can be seen further in Fig. 12 where we plot the phonon MFP vs phonon energy for the transport active acoustic + low-lying optic states. When the 250 nm thin-film scattering is turned on, a significant reduction in the MFP occurs, especially for the low-energy acoustic phonons. This is the reason for the corresponding reduction in the spectral κ in that energy range. We notice that for some states, the thin-film scattering does not affect the MFP. These are the states with a vanishing velocity component along the c axis. Consequently, these phonons continue to carry heat along the c plane despite the imposition of the thin-film boundary.

Lastly, in Fig. 13 we show the accumulation of the c plane κ as a function of MFP. The ph-iso scattering is included in all these calculations. The inclusion of the 4ph scattering on top of the 3ph scattering leads to a reduction of the total $\kappa_{\text{in-plane}}$ from 270 to 248 $\text{W m}^{-1} \text{K}^{-1}$, the last value being in good agreement with earlier experimental measurements on high purity, bulk samples with a natural isotopic mix [94]. For reference, we also give the corresponding $\kappa_{\text{cross-plane}}$ values for the 3ph and 3ph+4ph cases: 275 and 254 $\text{W m}^{-1} \text{K}^{-1}$, respectively. The anisotropy between the bulk thermal conductivities is low, with the in-plane value smaller than the cross-plane value by 1.8% and 2.4% for the 3ph and 3ph+4ph calculations, respectively. The 3ph+4ph calculation for the

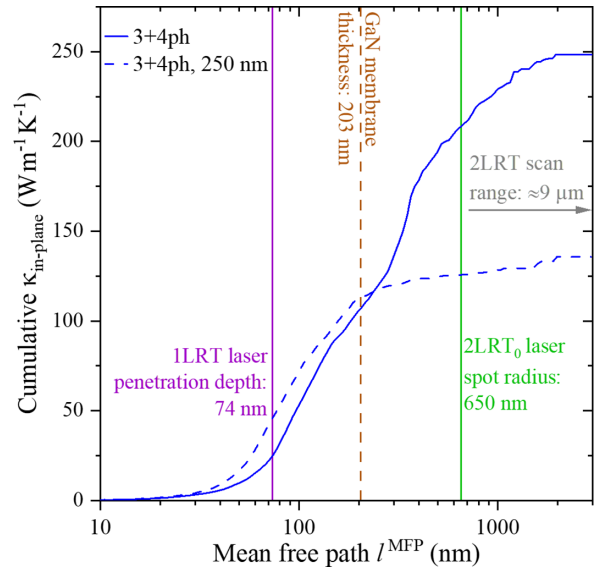


FIG. 13. $\kappa_{\text{in-plane}}$ accumulation with respect to phonon mean-free path l^{MFP} for an infinite crystal and a 250-nm-thick membrane. Phonon-isotope scattering is included in both cases (3ph+4ph and 3ph+4ph including boundary scattering). Vertical lines mark the relevant length scales r_{lim} of the 1LRT (purple) and 2LRT₀ (green) measurement techniques, while the gray arrow indicates the corresponding r_{lim} of 2LRT measurements. As r_{lim} of the 2LRT measurement is 9 μm , all relevant phonon mean-free paths are encompassed by the temperature probe volume in the GaN membrane. Additionally, a dashed vertical brown line indicates the GaN (without the AlN) membrane thickness.

250-nm-thin film case (dashed blue curve) is more relevant to our experimental observations. The calculated total $\kappa_{\text{in-plane}}$ in this case is 136 $\text{W m}^{-1} \text{K}^{-1}$. Again, for reference, the calculated total $\kappa_{\text{cross-plane}}$ is 89 $\text{W m}^{-1} \text{K}^{-1}$ in this case. The significantly stronger reduction of the $\kappa_{\text{cross-plane}}$ is due to the fact that the thin-film preferentially scatters phonons with large c -axis velocity component.

In Fig. 13 we mark with vertical lines the various limiting length scales r_{lim} of our experimental temperature probe volumes. This either corresponds to the penetration depth of the laser (p_{abs}) for the 1LRT measurements, the probe spot radius (r_{probe}) for the 2LRT₀ measurements, and the scanning range (r_{range}) of the 2LRT measurements beyond the limits of Fig. 13. Physically, in our experimental methods, these various lengths are phonon mean-free path visibility cutoffs. That is, the heat dissipation effects of any phonon with a mean-free path larger than r_{lim} cannot be detected. Thus, any measurement with r_{lim} shorter than the maximum phonon mean-free path will measure too large values of κ . Our theoretical calculations predict that in order to capture the heat dissipation effects of all the phonons in this material, r_{lim} must be at least 3 μm , which can only be met by 2LRT measurements as summarized in Sec. VIII via Fig. 14.

VIII. COMPARISON OF ONE- AND TWO-LASER RAMAN THERMOMETRY

Interestingly, based on 1LRT, 2LRT₀, and 2LRT thermometry we determined a continuous decline of the measured ther-

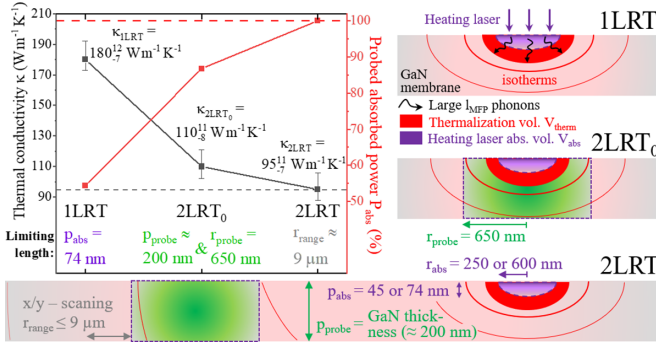


FIG. 14. Comparison of all thermal conductivities κ that were determined in this work. When increasing the probe volume, the measured κ values continuously decrease, starting with the highest value for 1LRT and ending with the lowest value for 2LRT measurements. The corresponding experimental situation for all three experimental techniques, namely 1LRT, 2LRT₀, and 2LRT, is sketched along with the related laser spot radii for the heating (r_{abs}) and the probe (r_{probe}) lasers. As the balance between the l^{MFP} values and the limiting length scales (p_{abs} , r_{probe} , and r_{range}) of the associated temperature probe volumes varies, the measured κ values are altered. In the end, only 2LRT measurements allow enclosing most l^{MFP} values in the thermalization volume, which leads to a realistic measure of $\kappa_{\text{memb}}^{2\text{LRT}}$. Due to the limited temperature probe volume, 1LRT and 2LRT₀ only probe effective and artificially enhanced κ values as only a fraction of P_{abs} is probed.

mal conductivities from $\kappa_{\text{memb}}^{1\text{LRT}} = 180_{-7}^{+12} \text{ W m}^{-1} \text{ K}^{-1}$, over $\kappa_{\text{memb}}^{2\text{LRT}_0} = 110_{-8}^{+11} \text{ W m}^{-1} \text{ K}^{-1}$, to $\kappa_{\text{memb}}^{2\text{LRT}} = 95_{-7}^{+11} \text{ W m}^{-1} \text{ K}^{-1}$ as summarized in Fig. 14. In the following, we first discuss the relevance of the absolute values that we determined for κ_{memb} in Sec. VIII A, before the evolution of κ_{memb} that depends on the Raman thermometry technique in use is discussed in Sec. VIII B.

A. Absolute value of the thermal conductivity

Based on our theoretical results presented in Sec. VII and literature values, only $\kappa_{\text{memb}}^{2\text{LRT}}$ represents a realistic value for our 253-nm-thick photonic membrane due to the dominance of phonon boundary scattering [75] that inhibits thermal transport. For GaN layers with a similar thickness, Beechem *et al.* [75] predicted a thermal conductivity of $\approx 70 \text{ W m}^{-1} \text{ K}^{-1}$ if phonon boundary scattering represents the main limiting factor for κ . However, even drastically lower κ values were predicted for the dislocation density in our photonic membrane of $3\text{--}4 \times 10^{10} \text{ cm}^{-2}$. In our membrane, anharmonic scattering, phonon-boundary scattering, i.e., size effects, isotope scattering, and phonon-dislocation scattering are potentially relevant limitations for thermal transport. Phonon-impurity scattering can only be of minor relevance due to the low impurity density ($< 10^{17} \text{ cm}^{-3}$) in our sample, cf. Sec. II A. Regarding the phonon-dislocation-scattering, Li *et al.* [83] have experimentally and theoretically demonstrated that the role of phonon-dislocation scattering is often overestimated in literature for GaN layers, as even for a dislocation density of $1.80 \times 10^{10} \text{ cm}^{-2}$ they measured $\kappa \approx 175 \text{ W m}^{-1} \text{ K}^{-1}$ for a 3.19- μm -thick GaN sample grown on AlN and sapphire. Nevertheless, as our photonic membrane

also includes 50 nm of AlN, we can expect that this interlayer can further boost thermal transport in our entire photonic membrane. The thermal conductivity of bulk AlN is commonly around 50% higher compared with bulk GaN at room temperature, when considering the natural abundance of isotopes [95], while the AlN in our epilayer contributes $\approx 20\%$ to the overall volume.

However, as the AlN buffer layer is grown on silicon (111), it is particularly rich in structural (e.g., dislocations) and point defects (e.g., silicon originating from diffusion from the substrate), which will further limit its thermal conductivity advantage compared with the GaN layer grown on top. In addition, with 50 nm the AlN layer is comparably thin, meaning that phonon-boundary scattering at the AlN-vacuum interface and phonon-interface scattering at the AlN-GaN interface, will significantly lower its thermal conductivity. Here, only future work can provide insight into the particular contribution of this AlN interlayer to the overall $\kappa_{\text{memb}}^{2\text{LRT}}$ value of $95_{-7}^{+11} \text{ W m}^{-1} \text{ K}^{-1}$, which we determined for our photonic membrane. Either depth-resolved thermometry based on frequency-domain thermal reflectance can be performed, or the AlN bottom layer must be removed by chemically selective wet etching. However, Rousseau [46] has shown that the removal of this tensile-strained AlN layer leads to the bowing of the rest of the photonic membrane, which renders it unusable for any photonic applications. Thus, such modification of the photonic membrane would counteract the motivation of this work to study structures with a high relevance for photonic applications from an optical and thermal viewpoint. In addition, the smooth top and bottom facets of our photonic membrane described in Sec. II A potentially lower the impact of phonon-boundary scattering on $\kappa_{\text{memb}}^{2\text{LRT}}$. Commonly, it is known that any interface roughness can have a strong impact on the thermal conductivity [96].

Regarding the absolute comparison between our experimental value $\kappa_{\text{memb}}^{2\text{LRT}} = 95_{-7}^{+11} \text{ W m}^{-1} \text{ K}^{-1}$ and its theoretical counterpart $\kappa_{\text{in-plane}} = 136 \text{ W m}^{-1} \text{ K}^{-1}$ from Sec. VII, it is important to mention that our theory only predicts an upper bound for the thermal conductivity. In this work, we refrain from implementing the impact of dislocations for the following reasons: (a) The impact of dislocations on the thermal conductivity of GaN was lately strongly debated in literature [75,83] and theoretical work by Wang *et al.* [97] has predicted a minor impact of dislocations in GaN layers up to $\approx 10^{10} \text{ cm}^{-2}$. Thus, in a photonic membrane with a thickness of $\approx 250 \text{ nm}$ one can expect that phonon-boundary scattering will dominate scattering in samples with a dislocation density of $3\text{--}4 \times 10^{10} \text{ cm}^{-2}$, cf. Sec. II. (b) Additionally the preferential alignment of dislocations in our *c*-plane GaN membrane would need to be considered in a more advanced theory, which represents an interesting task for a future sample series with varying dislocation densities. Furthermore, we can expect that not only the consideration of phonon-dislocation scattering but also the theoretical treatment of thermal transport across the interfaces of our pad structure (GaN-InGa_N, GaN-AlN, AlN-Si interfaces) would further close the gap between our theoretical value $\kappa_{\text{in-plane}}$ and its experimental counterpart $\kappa_{\text{memb}}^{2\text{LRT}}$. Here a model based on Green's function [98] could be employed to model the interfacial thermal transport. Future

work may be devoted to understand and quantify the relative contributions of these effects.

B. Scaling of the thermal conductivity

The particular scaling for the derived κ values as one of the main results of this work can be explained by considering the temperature probe volume. For this matter, Fig. 14 summarizes the experimental situation for 1LRT, 2LRT₀, and 2LRT measurements in three sketches that highlight the main length scales that limit the temperature probe volume.

1. One-laser Raman thermometry

For 1LRT measurements the volume in which the power of the heating laser is absorbed coincides with the temperature probe volume as a first approximation. This volume is the origin of the resonant Raman spectra that are used to determine the local temperature. Here, the heating laser spot radius r_{abs} measures 600 ± 50 nm, while the light penetration depths p_{abs} yields 74 nm [69]. Thus, the main size limit for the temperature probe volume for 1LRT measurements is oriented in the cross-plane direction, as a significant fraction of heat-carrying phonons with $l^{\text{MFP}} > p_{\text{abs}}$ exists that still contributes to the overall κ of the sample, cf. Fig. 13. A certain fraction of all the generated heat-carrying phonons travels quasiballistically and the first scattering event that starts their thermalization occurs outside the 1LRT temperature probe volume $V_{\text{probe}}^{\text{expt}}$, creating a thermalization volume $V_{\text{therm}}^{\text{expt}}$ that is larger than the light absorption volume $V_{\text{abs}}^{\text{expt}}$, with $V_{\text{abs}}^{\text{expt}} = V_{\text{probe}}^{\text{expt}}$ for 1LRT.

The problem occurs when the thermal conductivity $\kappa_{\text{memb}}^{\text{1LRT}}$ is extracted based on the comparison to our Fourier-based model described in Sec. V A. Even though we precisely consider all experimental parameters (e.g., p_{abs} , r_{probe} , P_{abs}) for such a model, the calculated T_{rise} will always exceed the experimental T_{rise} values due to the reduced thermalization volume $V_{\text{therm}}^{\text{sim}}$ in the simulation of 1LRT measurements. Since no model exists that accounts for the extended $V_{\text{therm}}^{\text{expt}}$ (even based on the results presented in Sec. VII), our analysis of the 1LRT data is always limited to

$$1LRT : V_{\text{abs}}^{\text{sim,expt}} = V_{\text{probe}}^{\text{sim,expt}} = V_{\text{therm}}^{\text{sim}} \ll V_{\text{therm}}^{\text{expt}}.$$

Consequently, based on our model for 1LRT measurements that aims to match the calculated T_{rise} values to the experimental ones, we always determine artificially enhanced $\kappa_{\text{memb}}^{\text{1LRT}}$ values, cf. Fig. 14.

2. Two-laser Raman thermometry

The situation is improved as soon as we transition from 1LRT to 2LRT₀ measurements that probe the entire GaN membrane thickness through nonresonant Raman scattering. Here the temperature probe volume in the cross-plane direction is limited by the GaN fraction of the membrane and for all in-plane directions by the radius $r_{\text{probe}} = 600 \pm 50$ nm of the temperature probe laser spot, cf. Fig. 14. As a result, a much larger fraction of the thermalization volume is measured in the temperature probe volume of 2LRT₀ measurements, leading to

$$2LRT_0 : V_{\text{abs}}^{\text{sim,expt}} = V_{\text{therm}}^{\text{sim}} < V_{\text{probe}}^{\text{sim,expt}} < V_{\text{therm}}^{\text{expt}}.$$

As a result, we obtain a $\kappa_{\text{memb}}^{\text{2LRT}_0}$ value that is significantly lower than $\kappa_{\text{memb}}^{\text{1LRT}}$ (see Fig. 14), which already compares well to previously published results [75]. Nevertheless, a small fraction of heat-carrying phonons still exists that exhibits $l^{\text{MFP}} > r_{\text{probe}}$, which in turn also artificially enhances $\kappa_{\text{memb}}^{\text{2LRT}_0}$. However, compared with the strong artificial increase of $\kappa_{\text{memb}}^{\text{1LRT}}$, this enhancement is minor as the majority of heat-carrying phonons thermalizes in $V_{\text{probe}}^{\text{sim,expt}}$ at $T_{\text{amb}} = 295$ K, cf. Figs. 13 and 14.

By further enlarging the temperature probe volume based on 2LRT measurements over $r_{\text{range}} \leq 9$ μm , all relevant l^{MFP} values are comprised in the temperature probe volume:

$$2LRT : V_{\text{abs}}^{\text{sim,expt}} = V_{\text{therm}}^{\text{sim}} < V_{\text{therm}}^{\text{expt}} \ll V_{\text{probe}}^{\text{sim,expt}}.$$

Now that the temperature probe volume encompasses the entire thermalization volume, the extraction of the thermal conductivity based on our Fourier model leads to our final thermal conductivity $\kappa_{\text{memb}}^{\text{2LRT}} = 95_{-7}^{+11}$ $\text{W m}^{-1} \text{K}^{-1}$. The fraction of P_{abs} that is measured in the temperature probe volume of all three experimental techniques is reported in Fig. 14, along with the main extensions p_{abs} , r_{probe} , and r_{range} that predominantly limit the temperature probe volume during our Raman thermometry. These extensions then enable the comparison to our results of *ab initio* calculations shown in Fig. 13.

3. Choice of heating laser

Let us note that we applied a cw 325 nm heating laser for our 1LRT measurements and a cw 266 nm heating laser for our 2LRT₀ and 2LRT measurements. The reason for this choice is twofold. First, based on our 266 nm laser we were not able to acquire high quality resonant Raman spectra for 1LRT measurements. Despite the high ultraviolet sensitivity of our experimental setup, even integration times of 10 min per resonant Raman spectrum did not yield a solid data basis. Thus, we transitioned to a 325 nm cw laser for 1LRT measurements, utilizing a microscope objective optimized for this wavelength. However, for 2LRT₀ and 2LRT measurements, we still applied our 266 nm cw laser due to the larger available range for P_{abs} , but also the dual-wavelength range design of our main microscope objective. This particular microscope objective is optimized around 266 nm and the visible range around 500 nm (high transmission and overlapping focal planes), but exhibits poor transmission at 325 nm ($\leq 15\%$). Thus, the light penetration depth for the heating laser changes from $p_{\text{abs}} = 74$ nm [69] for 1LRT measurements to $p_{\text{abs}} = 45$ nm [69] for 2LRT₀ and 2LRT measurements. However, this change in p_{abs} will not affect the overall trend for all three κ values in Fig. 14. On the contrary, the overestimation of $\kappa_{\text{memb}}^{\text{1LRT}}$ should even be more pronounced for a 266 nm heating laser.

IX. DISCUSSION AND OUTLOOK

As a result of Fig. 14, 2LRT measurements appear as the only suited method to measure κ in our photonic membrane made from III-nitride material. Still 1LRT measurements could also be applied to measure realistic values for κ . But for this purpose, the laser spot size and laser penetration depth would need to be tuned in a way such that their corresponding length scales ($r_{\text{probe}} \approx r_{\text{abs}}$ and $p_{\text{probe}} \approx p_{\text{abs}}$) are sufficient to

probe the major fraction of heating carrying phonons that significantly contribute to κ , cf. Fig. 13. Let us note, however, that for direct band gap semiconductors like GaN whose absorption coefficient exceeds $1 \times 10^5 \text{ cm}^{-1}$ above the band edge [76], this remains a challenging task. To achieve larger p_{probe} values for 1LRT measurements in GaN, one would need to tune the laser wavelength around the onset of absorption in close energetic proximity to the band edge [65]. However, in this energetic regime the absorption features of band-to-band transitions and excitons still overlap (e.g., at $T_{\text{amb}} = 295 \text{ K}$), rendering any precise determination of P_{abs} a challenging task. This is especially true for the comparably large T_{rise} values common for Raman thermometry [29]. As soon as temperatures are so drastically increased, the energetically steep absorption onset of excitons and/or band-to-band transitions shifts towards lower energies [99], which in turn varies the absorption. In addition, depending on the local temperature, the balance between the different contributions to the absorption is altered. As a result of these thermal nonlinearities, one lacks a constant value for the absorption coefficient at a fixed heating wavelength, which prevents any meaningful 1LRT measurements. In general, changes in the absorption coefficient are less pronounced deeper in the bands of a direct band gap semiconductor compared with the region close to its band edge. Nevertheless, for large values of T_{rise} , the absorption coefficient at a certain wavelength cannot always be considered as constant, even when the energetic spacing to the band edge is increased. Clearly, such optical nonlinearities remain an interesting task for future work. Potential optical nonlinearities related to the absorption coefficient are another reason why we refrain from performing a more detailed analysis of the high-temperature data shown in Figs. 4 and 5 ($> 150 \text{ K}$). Interestingly, the high absorption coefficient of GaN that complicates the Raman thermometry is directly connected to the reason why GaN has such a high relevance for photonic applications, which commonly rely on direct band gap semiconductors for emitters.

For the thermal characterization via TDTR measurements, it is common practice to work with sufficiently large and well-defined laser spot diameters [83] on the order of several tens of micrometers. At the same time, the light penetration depths is less problematic compared with our Raman thermometry technique as usually metal transducers made from, e.g., gold, aluminum, and silver are employed. On the one hand, this makes TDTR measurements a quantitative, reliable, and consequently well-established thermal technique. On the other hand, the complications that arise for Raman thermometry also carry a strong potential for measuring the mean-free path length of heat-carrying phonons and their impact on κ . By controlling the heat and probe laser spot diameters during transient thermoreflectance (TTR) measurements, Minnich *et al.* have pioneered such phonon mean-free path lengths measurements in silicon [37]. Interestingly, our results suggest that Raman thermometry could, similarly to TTR measurements, be suited for measuring phonon mean-free path lengths, which is particularly promising due to the experimental simplicity of Raman spectroscopy compared with pump-probe techniques. Clearly, this potential for measuring heat-carrying phonon mean-free path lengths adds to the overall interesting aspects of 2LRT measurements that

were shown in this work. Not only that a high spatial resolution can be achieved by our noninvasive experimental technique, but also the full angular dependence of κ in highly nonsymmetric semiconductors like $\beta\text{-Ga}_2\text{O}_3$ [100,101] could readily be explored. In addition, as in TDTR and micro-TDTR [24] measurements, Raman thermometry carries the potential for measurements at cryogenic temperatures. Still, the temperature limits of Raman thermometry for GaN and AlN need to be explored in full detail. Furthermore, our 2LRT measurements could even represent an interesting alternative to other noninvasive thermometry techniques like thermal transient grating (TTG) spectroscopy [102]. Thanks to the spatial resolution of 2LRT measurements one could potentially directly witness effects of non-Fourier-like thermal transport in real-space, such as a negative local effective thermal conductivity: close to the material's edge, the heat flux may have the same sign as the temperature gradient—a clear violation of Fourier's law [103]. Therefore, our experimental setup may open up exciting opportunities to probe these effects, while remaining nonintrusive.

A. Comparison with transient thermoreflectance

The direct comparison between the pioneering TTR work of Minnich *et al.* [37] and our Raman thermometry measurements summarized in Fig. 14 implies some additional insights into two different experimental perspectives on thermal transport as soon as the length scale of the heated volume in a bulk semiconductor approaches the mean-free path lengths of the heat-carrying phonons l^{MFP} .

First, we start with a brief summary of the findings of Minnich *et al.* [37]. Below an ambient temperature of 200 K they found that the effective thermal conductivity measured on high-quality bulk silicon declined with the diameter of their heater scaling from 60–15 μm ($1/e^2$ definition of the diameter). For these TTR measurements, the heater is given by an Al transducer that is heated by a focused laser. This transducer is also used to measure the evolution of temperature via its relative reflectivity changes $\Delta R/R$ probed by a second laser. As this is a transient experiment, $\Delta R/R$ declines (specific to the choice of the metal transducer and probe laser wavelength) over time, which can be recorded in a, so-called, thermal transient. Subsequently, relevant material parameters like, e.g., κ can be derived from these transients by comparison to a Fourier-based dynamic model that originates from the time-dependent heat equation [104]. The interpretation of their findings is relying on the assumption that the phonon bath can be divided into a purely diffusive and purely ballistic fraction, which represents a well-justified simplification. When lowering the diameter of their laser heat spot on the metal transducer (i.e., the heater) in comparison to a smaller and constant probe spot diameter (11 μm), they measure the most pronounced decline of effective κ values at, e.g., an ambient temperature of 60 K. This decline is then attributed to an increasingly large fraction of heat-carrying phonons that propagates ballistically. In the approximation of Minnich *et al.* this subgroup of phonons undergoing ballistic transport does not contribute to thermal transport, in contrast with the subgroup of diffusively propagating thermal phonons that they predominantly probe by their TTR experiment (regulated by

the diameters of the heat and probe laser spots). As a result, the heat flux from the perspective of their transient temperature probe is lower than predicted by Fourier's law, which is then interpreted as a ballistic thermal resistance. Finally, the increase of this ballistic thermal resistance with decreasing diameter of their heater leads to the measurement of an effective reduction of κ at ≤ 200 K in silicon.

As good experimental practice, during the reduction of the heater diameter the laser power density was kept constant on the surface of the metal transducer during the TTR experiments. Consequently, an identical temperature rise should have been achieved in the Al transducer. However, due to the reduction of the diameter of the heat spot, this does not necessarily lead to the same temperature rises in the silicon material underneath, when transitioning to an increasingly ballistic regime of thermal phonon transport. Here, the ratio between the heat and probe laser focus spot diameters will impact the temporal evolution of the diminishing temperature rises (i.e., local cooling) that are indirectly measured via $\Delta R/R$ for ambient temperatures ≤ 200 K. Thus, for the interpretation of the TTR measurements the problem already arises when translating $\Delta R/R$ values to temperature rises in the material located underneath the metal transducer based on the oversimplified model given by the time-dependent heat equation. Based on this model, the thermal transients provide access to the thermal flux, while the temperature gradient around the heat spot in silicon is overestimated, resulting in a decline of the effective κ values with diminishing diameter of the heater. Thus, for TTR measurements the challenge rests in the direct determination of the temperature rise in the material as soon as the dimension of the heater approaches the l^{MFP} values of a significant fraction of the heat-carrying phonons.

In this regard, our Raman thermometry technique can provide an interesting additional perspective as, e.g., 1LRT measurements probe absolute temperature rises directly in the material of choice at the cost of all complications that come along with an optical heating of a sample, cf. Sec. V A. For our 1LRT measurements with the smallest achievable temperature probe volume, we directly measure a temperature rise that is overestimated by our numerical model based on the stationary heat equation and Gaussian surface heating, cf. S-Sec. IV [47]. This small temperature rise is then interpreted as a sign of high thermal conductivity within the limitations of Fourier's law. Thus, despite the fact that Raman thermometry can probe (here, steady state) temperature rises directly in the sample region of interest, it still suffers from the application of oversimplified modeling. The analysis of TTR measurements from Minnich *et al.* leads to a reduction of the thermal flux with decreasing heat spot size, which is translated into a reduction of effective κ values by a Fourier-based model. In contrast, we directly observe an absolute lowering of the temperature rise in the temperature probe volume of 1LRT measurements when compared to our Fourier-based model, which is misinterpreted as being caused by a large thermal flux due to a large κ value.

However, the approach adopted by TTR and Raman thermometry to measure realistic κ values within the corset of a Fourier-based model is similar. By increasing the diameter of the heater during TTR measurements increasingly larger effective values for κ are measured until a realistic value is

reached by comprising the most significant fraction of l^{MFP} of all heating carrying phonons in the experiment. For Raman thermometry the same happens when the temperature probe volume is increased (transition from 1LRT, through 2LRT₀, and finally to 2LRT). Smaller and smaller effective values for κ are measured, until a realistic value for κ is obtained. Finally, this interesting comparison of TTR measurements and Raman thermometry directly illustrates the need for more appropriate modeling to take advantage of any direct temperature measurement enabled by Raman thermometry. Nevertheless, both experimental techniques provide promising experimental access to the l^{MFP} distribution of all heat-carrying phonons.

B. Photogenerated carriers

In general, the main challenge with Raman thermometry is the complicated generation of heat via the absorption of laser light. Not only heat-carrying phonons are generated and contribute to κ , but also free carriers and excitons can be generated. Consequently, depending on the sample quality and T_{amb} , a complicated balance of different contributions remains to be disentangled. In this contribution, we simplified this problem by characterizing a particularly suited photonic membrane by 2LRT measurements, which allowed us to focus on thermal transport dominated by heat-carrying phonons. All these potential additional contributions to thermal transport also render 2LRT measurements advantageous over 1LRT measurements, as the potentially complicated area where the laser light is absorbed can be excluded from the thermal characterization. Thus, the analysis of 2LRT data can begin, e.g., several micrometers away from the heating spot, which is in many direct band gap semiconductors enough to exclude a dominant contribution of excitons and carrier transport to thermal transport as mean-free path lengths are—in the best-case scenario—limited by the radiative lifetime of these excitations [36]. However, this simplification cannot be taken for granted in indirect band gap semiconductors of sufficiently high crystalline quality, which can exhibit comparably longer mean-free path lengths for excitons and carriers.

Furthermore, we can exclude that our trend for the κ values extracted from 1LRT, 2LRT₀, and 2LRT measurements (see Fig. 14) is predominantly impacted by photogenerated carriers. For the 2LRT measurements, this argument trivially holds as the probed temperature region is sufficiently far from the laser-induced heating spot in comparison to the mean carrier diffusion length $l_{\text{diff}} \leq 60$ nm in our sample, cf. Sec. II and S-Sec. II. See the top axis of Fig. 7(a) regarding the distance of the temperature probe region to the heating spot. In our 1LRT and 2LRT₀ measurements the situation is more complicated, yet we can estimate an upper bound for the photogenerated carrier concentration in our photonic membrane. At $T_{\text{amb}} = 295$ K we measured an effective lifetime of $\tau_{\text{QW}} = 60 \pm 5$ ps for the QW transition ($E_1 = 2.75$ eV) in our sample based on time-resolved PL (TRPL) measurements [46]. Commonly, the carrier lifetime τ_{GaN} in the GaN matrix material that surrounds the QW is even lower as the QW traps the carriers. However, direct TRPL measurements on the band-edge emission of GaN ($E_2 = 3.41$ eV) at $T_{\text{amb}} = 295$ K were not feasible due to the low intensity of this band, which is caused by the intended

carrier transfer to the QW. Thus, based on $\tau_{\text{GaN}} < \tau_{\text{QW}}$ and the corresponding excitation and temperature probe volumes, we can estimate an upper bound for the photogenerated carrier concentration that is achieved during our 1LRT and 2LRT₀ measurements. During our 1LRT measurements shown in Fig. 4, at the largest $T_{\text{rise}} = 780 \pm 30$ K ($P_{\text{abs}} = 13.5$ mW), we reach the maximal number of photogenerated carriers with a concentration $\rho_{\text{1LRT}}^{\text{photo}} \approx 1.7 \times 10^{19}$ cm⁻³ in the temperature probe volume. Clearly, if not photoexcited, such high carrier concentration can only be achieved by heavy doping of GaN [105]. Let us note that this concentration represents an upper bound for $\rho_{\text{1LRT}}^{\text{photo}}$, because τ_{GaN} and τ_{QW} decline with increasing temperature due to the impact of nonradiative defects. At the same time with rising temperature the concentration of purely thermally excited free carriers also rises in GaN. The situation regarding the photoexcited carriers is similar for our 2LRT₀ measurements. However, due to the larger temperature probe volume we reach $\rho_{\text{2LRT}_0}^{\text{photo}} \approx 3.2 \times 10^{18}$ cm⁻³ at $T_{\text{rise}} = 730 \pm 130$ K ($P_{\text{abs}} = 9.3$ mW). Thus, any future detailed analysis of the full T_{rise} trends that we show for 1LRT and 2LRT₀ measurements in Figs. 4 and 5 will require temperature-dependent TRPL measurements in order to be conclusive. However, since we focus on $T_{\text{rise}} \leq 150$ K in this work to extract all κ values, the photogenerated carrier concentrations decrease. For this lower value of T_{rise} , we obtain upper bounds for the photogenerated carrier concentrations of $\rho_{\text{1LRT}}^{\text{photo}} \approx 6.4 \times 10^{18}$ cm⁻³ and $\rho_{\text{2LRT}_0}^{\text{photo}} \approx 1.4 \times 10^{18}$ cm⁻³.

Overall, the phonon current and hence κ , can be degraded by the phonon-charge carrier interaction since this causes a transfer of momentum from the phonon system to the charge carrier system. However, the charge carriers themselves can also carry heat and contribute positively to the total κ . However, even in heavily doped semiconductors, the phonon contribution to κ completely dominates the charge carriers' contribution and any electron drag enhancement of the phonon κ has also been found to be negligible in GaAs [106], SiC [107], and Si [81,108]. For doped Si, Liao *et al.* analyzed the impact of free carriers and holes on κ based on first principles calculations [109]. For *n*-type silicon they predict a moderate reduction of κ in silicon of 2% to 7% for free-electron concentrations scaling from 1×10^{18} to 1×10^{19} cm⁻³ due to the electron-phonon interaction. In GaN this electron-phonon interaction is enhanced due to the polar nature of acoustic phonons, which has already motivated several theoretical studies in this field [110–113]. Accordingly, a reduction of κ with rising carrier concentration is commonly reported for homogeneously doped samples, which contradicts the experimental trend that we observe for our Raman thermometry measurements summarized in Fig. 14. Thus, as we observe a decrease in κ with decreasing density of photogenerated carriers in the temperature probe volume, scaling from 1LRT, over 2LRT₀, to 2LRT measurements, we can exclude any prominent impact of photogenerated carriers on κ in our photonic membrane.

It nonetheless remains an interesting task to probe κ over the full range of experimentally accessible T_{rise} values in, e.g., GaN membranes of even higher quality in comparison with the sample that formed the basis for this work. Here, GaN membranes that originate from GaN grown on sapphire

or even bulk GaN substrates could be appropriate platforms [114]. In such samples even higher values for τ_{GaN} and τ_{QW} can be expected, potentially leading to even higher achievable photogenerated carrier concentrations with a stronger impact on κ and its temperature dependence. It also remains an interesting open question how a local photoexcitation-induced carrier distribution can be compared with global carrier distributions induced by, e.g., doping and/or thermal excitation.

X. SUMMARY

In summary, we show how quantitative and noninvasive thermometry by optical means can be achieved by spatially resolved 2LRT measurements on a photonic semiconductor membrane made from III nitrides. Thanks to the spatial resolution of the 2LRT technique, the analysis of temperature gradients in such a membrane can be limited to regions sufficiently far from the heating spot and the heat sink, which simplifies the data analysis. This simplification goes hand-in-hand with the possibility to disentangle different contributions to thermal transport given by, e.g., charge carriers and heat-carrying phonons by their deviating mean-free paths. Interestingly, we demonstrated 2LRT measurements on a partially under-etched photonic membrane, which using a very similar geometry has already formed the basis for nanolasers [10,42–46]. Consequently, our thermal analysis of the most fundamental building block of such nanolasers can constitute the basis for future thermal optimizations of these structures. For thermometry that applies a laser as the heat source, such light-emitting structures inflict the particular challenge of a precise determination of the heating power because part of the absorbed laser power is converted to light in the In_xGa_{1-x}N/GaN ($x = 0.15$) QW structure that forms the core of our photonic membrane. Thus, based on our interlinked thermal and optical analysis in our fully customized optical setup, we showed that we can safely neglect the energy loss by the emission of photons. Furthermore, our experimental setup pioneers an approach for 2LRT measurements that only requires front-side access of the sample—a technical, but still relevant step regarding the applicability of 2LRT measurements to a large variety of samples. Commonly photonic membranes are never fully under-etched, which renders 2LRT measurements a preferential choice for their analysis, which is further strengthened by the fact that no metal transducer is required as for most alternative, reflectivity-based techniques.

Experimentally we introduced our 2LRT measurements in a step-by-step approach starting with 1LRT and 2LRT₀ measurements, exhibiting different heat and temperature probe volumes and a differing sensitivity to thermally induced stress. Based on *ab initio* calculations of phonon transport we show that 1LRT measurements always overestimate κ in our sample due to an insufficient size of the temperature probe volume. For these calculations, we took into account the main limiting factors of phonon transport in our photonic membrane, which comprises three- and four-phonon-scattering, phonon-isotope scattering, as well as phonon boundary scattering. As an outcome of this theory of phonon transport in a photonic membrane, we were also able to elucidate an intriguing scaling behavior for κ . From 1LRT to 2LRT₀ to 2LRT measurements, the temperature probe volume increases, which is

accompanied by a systematic decrease of κ . Based on the phonon mean-free path lengths obtained from our calculations, we showed that only 2LRT measurements allow us to encompass the entire set of heat-carrying phonons that contributes to κ . This result is a central aspect of this work, as it opens the perspective for phonon mean-free path spectroscopy based on a systematic variation of the temperature probe volume used for Raman thermometry. Precise control over the heated volume and the temperature probe volume is especially relevant for direct band-gap semiconductors often used for photonic applications due to the occurrence of absorption coefficients at the wavelength of the heat laser. Consequently, 1LRT measurements can only provide quantitative results, if the temperature probe volume defined by the absorption depth of the Raman laser and its focus diameter are carefully adapted to the distribution of phonon mean-free paths at the temperature of interest. Otherwise, 1LRT measurements will always lead to an overestimation of κ , which seems especially relevant for nanostructures that are challenging to probe with alternative thermometric techniques. Here, the quasiballistic transport of heat-carrying phonons at room temperature in, e.g., GaN poses a general challenge to Raman thermometry aiming for high spatial resolution, while maintaining the aim of a precise measure of κ . Therefore, 2LRT measurements provide a generally promising alternative, as the entire spatial

temperature distribution across the sample can be probed. For future work, it is of utmost importance to directly model these experimental temperature distributions. Consequently, the comparison to calculations will no longer be limited to a comparison of κ values but extended to a direct comparison with non-Fourier-like temperature maps. This point is even further strengthened by the possibility to measure 2LRT down to cryogenic temperatures, which will give direct experimental access to different phonon transport regimes by temperature imaging.

ACKNOWLEDGMENTS

N.H.P. was supported by a Humboldt Research Fellowship from the Alexander von Humboldt Foundation, Bonn, Germany. M.E. and G.C. acknowledge funding from the Central Research Development Fund (CRDF) of the University of Bremen for the project “Joined optical and thermal designs for next generation nanophotonics.” The research of M.E., W.S., K.D., D.V., and G.C. was funded by the Deutsche Forschungsgemeinschaft (DFG, German Research Foundation) - 511416444. G.R. acknowledges MIT-IBM Watson AI Laboratory (Challenge No. 2415). This work was supported by the Swiss National Science Foundation through Grants No. 200020_162657 and No. 200021E_175652.

-
- [1] Z. Fan, An analysis of GaN-based ultraviolet photodetector, *IOP Conf. Ser.: Mater. Sci. Eng.* **738**, 012006 (2020).
- [2] M. A. H. Khan and M. V. Rao, Gallium nitride (GaN) nanostructures and their gas sensing properties: A review, *Sensors* **20**, 3889 (2020).
- [3] M. Kneissl, T.-Y. Seong, J. Han, and H. Amano, The emergence and prospects of deep-ultraviolet light-emitting diode technologies, *Nat. Photonics* **13**, 233 (2019).
- [4] M. Kneissl, Z. Yang, M. Teepe, C. Knollenberg, O. Schmidt, P. Kiesel, N. M. Johnson, S. Schujman, and L. J. Schowalter, Ultraviolet semiconductor laser diodes on bulk AlN, *J. Appl. Phys.* **101**, 123103 (2007).
- [5] S. Nakamura, M. Senoh, S.-ichi Nagahama, N. Iwasa, T. Yamada, T. Matsushita, K. Hiroyuki, and S. Yasunobu, InGaN-based multi-quantum-well-structure laser diodes, *Jpn. J. Appl. Phys.* (1962–1981) **35**, L74 (1996).
- [6] M. Kneissl, D. W. Treat, M. Teepe, N. Miyashita, and N. M. Johnson, Ultraviolet AlGaIn multiple-quantum-well laser diodes, *Appl. Phys. Lett.* **82**, 4441 (2003).
- [7] F. Nippert, S. Yu. Karpov, G. Callsen, B. Galler, T. Kure, C. Nenstiel, M. R. Wagner, M. Straßburg, H.-J. Lugauer, and A. Hoffmann, Temperature-dependent recombination coefficients in InGaN light-emitting diodes: Hole localization, Auger processes, and the green gap, *Appl. Phys. Lett.* **109**, 161103 (2016).
- [8] M. Sheen, Y. Ko, D.-u. Kim, J. Kim, J.-h. Byun, Y. Choi, J. Ha, K. Y. Yeon, D. Kim, J. Jung, J. Choi, R. Kim, J. Yoo, I. Kim, C. Joo, N. Hong, J. Lee, S. H. Jeon, S. H. Oh, J. Lee, N. Ahn, and C. Lee, Highly efficient blue InGaN nanoscale light-emitting diodes, *Nature (London)* **608**, 56 (2022)..
- [9] F. Nippert, M. Tollabi Mazraehno, M. J. Davies, M. P. Hoffmann, H.-J. Lugauer, T. Kure, M. Kneissl, A. Hoffmann, and M. R. Wagner, Auger recombination in AlGaIn quantum wells for UV light-emitting diodes, *Appl. Phys. Lett.* **113**, 071107 (2018).
- [10] S. T. Jagsch, N. V. Triviño, F. Lohof, G. Callsen, S. Kalinowski, I. M. Rousseau, R. Barzel, J.-F. Carlin, F. Jahnke, R. Butté, C. Gies, A. Hoffmann, N. Grandjean, and S. Reitzenstein, A quantum optical study of thresholdless lasing features in high- β nitride nanobeam cavities, *Nat. Commun.* **9**, 564 (2018).
- [11] B. Gesemann, S. L. Schweizer, and R. B. Wehrspohn, Thermal emission properties of 2D and 3D silicon photonic crystals, *Photon. Nanostruct.* **8**, 107 (2010).
- [12] P. Wen, P. Tiwari, M. Scherrer, E. Lörtscher, B. Gotsmann, and K. E. Moselund, Thermal simulation and experimental analysis of optically pumped InP-on-Si micro- and nanocavity lasers, *ACS Photon.* **9**, 1338 (2022).
- [13] M. Aspelmeyer, T. J. Kippenberg, and F. Marquardt, Cavity optomechanics, *Rev. Mod. Phys.* **86**, 1391 (2014).
- [14] D. G. Cahill, K. Goodson, and A. Majumdar, Thermometry and thermal transport in micro/nanoscale solid-state devices and structures, *J. Heat Transfer* **124**, 223 (2002).
- [15] Y. Quan, S. Yue, and B. Liao, Impact of electron-phonon interaction on thermal transport: A review, *Nanoscale Microscale Thermophys. Eng.* **25**, 73 (2021).
- [16] K. Wu, L. Rademaker, and J. Zaanen, Bilayer excitons in two-dimensional nanostructures for greatly enhanced thermoelectric efficiency, *Phys. Rev. Appl.* **2**, 054013 (2014).
- [17] A. Sood, E. Pop, M. Asheghi, and K. E. Goodson, The Heat Conduction Renaissance, in *2018 17th IEEE Intersociety Conference on Thermal and Thermomechanical Phenomena in Electronic Systems (ITherm)* (IEEE, San Diego, CA, 2018), pp. 1396–1402.

- [18] D. G. Cahill, Thermal conductivity measurement from 30 to 750 K: The 3ω method, *Rev. Sci. Instrum.* **61**, 802 (1990).
- [19] D. G. Cahill, P. V. Braun, G. Chen, D. R. Clarke, S. Fan, K. E. Goodson, P. Keblinski, W. P. King, G. D. Mahan, A. Majumdar, H. J. Maris, S. R. Phillpot, E. Pop, and L. Shi, Nanoscale thermal transport. II. 2003–2012, *Appl. Phys. Rev.* **1**, 011305 (2014).
- [20] E. Matatagui, A. G. Thompson, and M. Cardona, Thermoreflectance in semiconductors, *Phys. Rev.* **176**, 950 (1968).
- [21] K. Liu, J. Zhao, H. Sun, H. Guo, B. Dai, and J. Zhu, Thermal characterization of GaN heteroepitaxies using ultraviolet transient thermoreflectance, *Chin. Phys. B* **28**, 060701 (2019).
- [22] Y. Wang, J. Y. Park, Y. K. Koh, and D. G. Cahill, Thermoreflectance of metal transducers for time-domain thermoreflectance, *J. Appl. Phys.* **108**, 043507 (2010).
- [23] R. B. Wilson, B. A. Apgar, L. W. Martin, and D. G. Cahill, Thermoreflectance of metal transducers for optical pump-probe studies of thermal properties, *Opt. Express* **20**, 28829 (2012).
- [24] J. Maire, R. Anufriev, R. Yanagisawa, A. Ramiere, S. Volz, and M. Nomura, Heat conduction tuning by wave nature of phonons, *Sci. Adv.* **3**, e1700027 (2017).
- [25] A. Cepellotti, G. Fugallo, L. Paulatto, M. Lazzeri, F. Mauri, and N. Marzari, Phonon hydrodynamics in two-dimensional materials, *Nat. Commun.* **6**, 6400 (2015).
- [26] S. Lee, D. Broido, K. Esfarjani, and G. Chen, Hydrodynamic phonon transport in suspended graphene, *Nat. Commun.* **6**, 6290 (2015).
- [27] R. Anufriev, A. Ramiere, J. Maire, and M. Nomura, Heat guiding and focusing using ballistic phonon transport in phononic nanostructures, *Nat. Commun.* **8**, 15505 (2017).
- [28] T. Beechem, S. Graham, S. P. Kearney, L. M. Phinney, and J. R. Serrano, Invited article: simultaneous mapping of temperature and stress in microdevices using micro-Raman spectroscopy, *Rev. Sci. Instrum.* **78**, 061301 (2007).
- [29] T. Beechem, L. Yates, and S. Graham, Invited review article: Error and uncertainty in Raman thermal conductivity measurements, *Rev. Sci. Instrum.* **86**, 041101 (2015).
- [30] J. Jaramillo-Fernandez, E. Chavez-Angel, and C. M. Sotomayor-Torres, Raman thermometry analysis: Modelling assumptions revisited, *Appl. Therm. Eng.* **130**, 1175 (2018).
- [31] M. Kuball, Raman spectroscopy of GaN, AlGaIn and AlN for process and growth monitoring/control, *Surf. Interface Anal.* **31**, 987 (2001).
- [32] S. Sandell, E. Chávez-Ángel, A. El Sachat, J. He, C. M. Sotomayor Torres, and J. Maire, Thermoreflectance techniques and Raman thermometry for thermal property characterization of nanostructures, *J. Appl. Phys.* **128**, 131101 (2020).
- [33] M. Lax, Temperature rise induced by a laser beam, *J. Appl. Phys.* **48**, 3919 (1977).
- [34] J. Ciers, D. D. Solnyshkov, G. Callsen, Y. Kuang, J.-F. Carlin, G. Malpuech, R. Butté, and N. Grandjean, Polariton relaxation and polariton nonlinearities in nonresonantly cw-pumped III-nitride slab waveguides, *Phys. Rev. B* **102**, 155304 (2020).
- [35] S.-A. Biehs, Thermal heat radiation, near-field energy density and near-field radiative heat transfer of coated materials, *Eur. Phys. J. B* **58**, 423 (2007).
- [36] T. F. K. Weatherley, W. Liu, V. Osokin, D. T. L. Alexander, R. A. Taylor, J.-F. Carlin, R. Butté, and N. Grandjean, Imaging nonradiative point defects buried in quantum wells using cathodoluminescence, *Nano Lett.* **21**, 5217 (2021).
- [37] A. J. Minnich, J. A. Johnson, A. J. Schmidt, K. Esfarjani, M. S. Dresselhaus, K. A. Nelson, and G. Chen, Thermal conductivity spectroscopy technique to measure phonon mean free paths, *Phys. Rev. Lett.* **107**, 095901 (2011).
- [38] I.-K. Hsu, M. T. Pettes, M. Aykol, C.-C. Chang, W.-H. Hung, J. Theiss, L. Shi, and S. B. Cronin, Direct observation of heat dissipation in individual suspended carbon nanotubes using a two-laser technique, *J. Appl. Phys.* **110**, 044328 (2011).
- [39] J. S. Reparaz, E. Chavez-Angel, M. R. Wagner, B. Graczykowski, J. Gomis-Bresco, F. Alzina, and C. M. Sotomayor Torres, A novel contactless technique for thermal field mapping and thermal conductivity determination: Two-laser Raman thermometry, *Rev. Sci. Instrum.* **85**, 034901 (2014).
- [40] M. Sledzinska, B. Graczykowski, M. Placidi, D. S. Reig, A. E. Sachat, J. S. Reparaz, F. Alzina, B. Mortazavi, R. Quey, L. Colombo, S. Roche, and C. M. S. Torres, Thermal conductivity of MoS₂ polycrystalline nanomembranes, *2D Mater.* **3**, 035016 (2016).
- [41] B. Graczykowski, A. El Sachat, J. S. Reparaz, M. Sledzinska, M. R. Wagner, E. Chavez-Angel, Y. Wu, S. Volz, Y. Wu, F. Alzina, and C. M. Sotomayor Torres, Thermal conductivity and air-mediated losses in periodic porous silicon membranes at high temperatures, *Nat. Commun.* **8**, 415 (2017).
- [42] N. Vico Triviño, G. Rossbach, U. Dharamipathy, J. Levrat, A. Castiglia, J.-F. Carlin, K. A. Atlasov, R. Butté, R. Houdré, and N. Grandjean, High quality factor two dimensional GaN photonic crystal cavity membranes grown on silicon substrate, *Appl. Phys. Lett.* **100**, 071103 (2012).
- [43] N. V. Triviño, R. Butté, J.-F. Carlin, and N. Grandjean, Continuous wave blue lasing in III-nitride nanobeam cavity on silicon, *Nano Lett.* **15**, 1259 (2015).
- [44] I. Rousseau, I. Sánchez-Arribas, K. Shojiki, J.-F. Carlin, R. Butté, and N. Grandjean, Quantification of scattering loss of III-nitride photonic crystal cavities in the blue spectral range, *Phys. Rev. B* **95**, 125313 (2017).
- [45] I. Rousseau, G. Callsen, G. Jacopin, J.-F. Carlin, R. Butté, and N. Grandjean, Optical absorption and oxygen passivation of surface states in III-nitride photonic devices, *J. Appl. Phys.* **123**, 113103 (2018).
- [46] I. M. Rousseau, Ph.D. thesis, École Polytechnique Fédérale de Lausanne, 2018.
- [47] See Supplemental Material at <http://link.aps.org/supplemental/10.1103/PhysRevB.108.235313> for a detailed presentation of the experimental setup, for details regarding various experimental parameters, for the temperature calibration, and for a presentation of the numerical model used to extract the thermal conductivity.
- [48] W. Liu, J.-F. Carlin, N. Grandjean, B. Deveaud, and G. Jacopin, Exciton dynamics at a single dislocation in GaN probed by picosecond time-resolved cathodoluminescence, *Appl. Phys. Lett.* **109**, 042101 (2016).
- [49] S. Fukura, T. Mizukami, S. Odake, and H. Kagi, Factors determining the stability, resolution, and precision of a conventional Raman spectrometer, *Appl. Spectrosc.* **60**, 946 (2006).
- [50] M. Hocker, P. Maier, L. Jerg, I. Tischer, G. Neusser, C. Kranz, M. Pristovsek, C. J. Humphreys, R. A. R. Leute, D. Heinz, O. Rettig, F. Scholz, and K. Thonke, Determination of axial

- and lateral exciton diffusion length in GaN by electron energy dependent cathodoluminescence, *J. Appl. Phys.* **120**, 085703 (2016).
- [51] J. J. Olivero and R. L. Longbothum, Empirical fits to the Voigt line width: A brief review, *J. Quant. Spectrosc. Radiat. Transfer* **17**, 233 (1977).
- [52] G. Callsen, M. R. Wagner, T. Kure, J. S. Reparaz, M. Bügler, J. Brunmeier, C. Nenstiel, A. Hoffmann, M. Hoffmann, J. Tweedie, Z. Bryan, S. Aygun, R. Kirste, R. Collazo, and Z. Sitar, Optical signature of Mg-doped GaN: Transfer processes, *Phys. Rev. B* **86**, 075207 (2012).
- [53] U. Jahn, V. M. Kaganer, K. K. Sabelfeld, A. E. Kireeva, J. Lähnemann, C. Pfüller, T. Flissikowski, C. Chêze, K. Biermann, R. Calarco, and O. Brandt, Carrier diffusion in GaN: A cathodoluminescence study. I. Temperature-dependent generation volume, *Phys. Rev. Appl.* **17**, 024017 (2022).
- [54] N. V. Triviño, Ph.D. thesis, École Polytechnique Fédérale de Lausanne, 2015.
- [55] A. Krost and A. Dadgar, GaN-based optoelectronics on silicon substrates, *Mater. Sci. Eng., B* **93**, 77 (2002).
- [56] Eric Feltin, Ph.D. thesis, CRHEA/CNRS, 2003.
- [57] T. Palacios, F. Calle, M. Varela, C. Ballesteros, E. Monroy, F. B. Naranjo, M. A. Sánchez-García, E. Calleja, and E. Muñoz, Wet etching of GaN grown by molecular beam epitaxy on Si(111), *Semicond. Sci. Technol.* **15**, 996 (2000).
- [58] C. Haller, J.-F. Carlin, G. Jacopin, D. Martin, R. Butté, and N. Grandjean, Burying non-radiative defects in InGaN underlayer to increase InGaN/GaN quantum well efficiency, *Appl. Phys. Lett.* **111**, 262101 (2017).
- [59] E. Stock, Ph.D. thesis, Technische Universität Berlin, 2010.
- [60] H. Schömig, S. Halm, A. Forchel, G. Bacher, J. Off, and F. Scholz, Probing individual localization centers in an InGaN/GaN quantum well, *Phys. Rev. Lett.* **92**, 106802 (2004).
- [61] A. Hangleiter, F. Hitzel, C. Netzel, D. Fuhrmann, U. Rossow, G. Ade, and P. Hinze, Suppression of nonradiative recombination by V-Shaped Pits in GaInN/GaN quantum wells produces a large increase in the light emission efficiency, *Phys. Rev. Lett.* **95**, 127402 (2005).
- [62] M. Piccardo, C.-K. Li, Y.-R. Wu, J. S. Speck, B. Bonef, R. M. Farrell, M. Filoche, L. Martinelli, J. Peretti, and C. Weisbuch, Localization landscape theory of disorder in semiconductors. II. Urbach tails of disordered quantum well layers, *Phys. Rev. B* **95**, 144205 (2017).
- [63] G. Callsen, R. Butté, and N. Grandjean, Probing alloy formation using different excitonic species: The particular case of InGaN, *Phys. Rev. X* **9**, 031030 (2019).
- [64] J. Bai, T. Wang, and S. Sakai, Influence of the quantum-well thickness on the radiative recombination of InGaN/GaN quantum well structures, *J. Appl. Phys.* **88**, 4729 (2000).
- [65] G. Callsen, T. Kure, M. R. Wagner, R. Butté, and N. Grandjean, Excited states of neutral donor bound excitons in GaN, *J. Appl. Phys.* **123**, 215702 (2018).
- [66] E. Feltin, B. Beaumont, M. Laügt, P. de Mierry, P. Vennéguès, H. Lahèche, M. Leroux, and P. Gibart, Stress control in GaN grown on silicon (111) by metalorganic vapor phase epitaxy, *Appl. Phys. Lett.* **79**, 3230 (2001).
- [67] G. Callsen, J. S. Reparaz, M. R. Wagner, R. Kirste, C. Nenstiel, A. Hoffmann, and M. R. Phillips, Phonon deformation potentials in wurtzite GaN and ZnO determined by uniaxial pressure dependent Raman measurements, *Appl. Phys. Lett.* **98**, 061906 (2011).
- [68] B. Gil, *Physics of Wurtzite Nitrides and Oxides* (Springer, Heidelberg, 2014).
- [69] T. Kawashima, H. Yoshikawa, S. Adachi, S. Fuke, and K. Ohtsuka, Optical properties of hexagonal GaN, *J. Appl. Phys.* **82**, 3528 (1997).
- [70] T. Beechem, A. Christensen, S. Graham, and D. Green, Micro-Raman thermometry in the presence of complex stresses in GaN devices, *J. Appl. Phys.* **103**, 124501 (2008).
- [71] W. S. Li, Z. X. Shen, Z. C. Feng, and S. J. Chua, Temperature dependence of Raman scattering in hexagonal gallium nitride films, *J. Appl. Phys.* **87**, 3332 (2000).
- [72] C. J. Glassbrenner and G. A. Slack, Thermal conductivity of silicon and germanium from 3 K to the melting point, *Phys. Rev.* **134**, A1058 (1964).
- [73] H. S. Carslaw and J. C. Jaeger, *Conduction of Heat in Solids*, 2nd ed. (Oxford University Press, London, 1959).
- [74] R. J. Barlow, Asymmetric statistical errors, in *Statistical Problems in Particle Physics, Astrophysics and Cosmology* (Published by Imperial College Press and distributed by World Scientific Publishing Co., Oxford, 2006), pp. 56–59.
- [75] T. E. Beechem, A. E. McDonald, E. J. Fuller, A. A. Talin, C. M. Rost, J. P. Maria, J. T. Gaskins, P. E. Hopkins, and A. A. Allerman, Size dictated thermal conductivity of GaN, *J. Appl. Phys.* **120**, 095104 (2016).
- [76] J. F. Muth, J. H. Lee, I. K. Shmagin, R. M. Kolbas, H. C. Jr Casey, B. P. Keller, U. K. Mishra, and S. P. DenBaars, Absorption coefficient, energy gap, exciton binding energy, and recombination lifetime of GaN obtained from transmission measurements, *Appl. Phys. Lett.* **71**, 2572 (1997).
- [77] E. Chávez-Ángel, J. S. Reparaz, J. Gomis-Bresco, M. R. Wagner, J. Cuffe, B. Graczykowski, A. Shchepetov, H. Jiang, M. Prunnila, J. Ahopelto, F. Alzina, and C. M. Sotomayor Torres, Reduction of the thermal conductivity in free-standing silicon nano-membranes investigated by non-invasive Raman thermometry, *APL Mater.* **2**, 012113 (2014).
- [78] J. Očenášek and J. Voldřich, Raman thermometry: Effective temperature of the nonuniform temperature field induced by a Gaussian laser, *J. Appl. Phys.* **118**, 233104 (2015).
- [79] B. Stoib, S. Filser, J. Stötzel, A. Greppmair, N. Petermann, H. Wiggers, G. Schierning, M. Stutzmann, and M. S. Brandt, Spatially resolved determination of thermal conductivity by Raman spectroscopy, *Semicond. Sci. Technol.* **29**, 124005 (2014).
- [80] W. Li, J. Carrete, N. A. Katcho, and N. Mingo, ShengBTE: A solver of the Boltzmann transport equation for phonons, *Comput. Phys. Commun.* **185**, 1747 (2014).
- [81] N. H. Protik, C. Li, M. Pruneda, D. Broido, and P. Ordejón, The elphbolt *ab initio* solver for the coupled electron-phonon Boltzmann transport equations, *npj Comput. Mater.* **8**, 28 (2022).
- [82] S.-i. Tamura, Isotope scattering of dispersive phonons in Ge, *Phys. Rev. B* **27**, 858 (1983).
- [83] H. Li, R. Hanus, C. A. Polanco, A. Zeidler, G. Koblmüller, Y. K. Koh, and L. Lindsay, GaN thermal transport limited by the interplay of dislocations and size effects, *Phys. Rev. B* **102**, 014313 (2020).
- [84] J. Carrete, B. Vermeersch, A. Katre, A. van Roekeghem, T. Wang, G. K. H. Madsen, and N. Mingo, almaBTE: A solver

- of the space-time dependent Boltzmann transport equation for phonons in structured materials, *Comput. Phys. Commun.* **220**, 351 (2017).
- [85] B. Vermeersch, J. Carrete, and N. Mingo, Cross-plane heat conduction in thin films with ab-initio phonon dispersions and scattering rates, *Appl. Phys. Lett.* **108**, 193104 (2016).
- [86] P. Giannozzi, S. Baroni, N. Bonini, M. Calandra, R. Car, C. Cavazzoni, D. Ceresoli, G. L. Chiarotti, M. Cococcioni, I. Dabo, A. Dal Corso, S. De Gironcoli, S. Fabris, G. Fratesi, R. Gebauer, U. Gerstmann, C. Gougoussis, A. Kokalj, M. Lazzeri, L. Martin-Samos, N. Marzari, F. Mauri, R. Mazzarello, S. Paolini, A. Pasquarello, L. Paulatto, C. Sbraccia, S. Scandolo, G. Sclauzero, A. P. Seitsonen, A. Smogunov, P. Umari, and R. M. Wentzcovitch, QUANTUM ESPRESSO: A modular and open-source software project for quantum simulations of materials, *J. Phys.: Condens. Matter* **21**, 395502 (2009).
- [87] P. Giannozzi, O. Andreussi, T. Brumme, O. Bunau, M. Buongiorno Nardelli, M. Calandra, R. Car, C. Cavazzoni, D. Ceresoli, M. Cococcioni, N. Colonna, I. Carnimeo, A. Dal Corso, S. De Gironcoli, P. Delugas, R. A. DiStasio Jr, A. Ferretti, A. Floris, G. Fratesi, G. Fugallo, R. Gebauer, U. Gerstmann, F. Giustino, T. Gorni, J. Jia, M. Kawamura, H.-Y. Ko, A. Kokalj, E. Küçükbenli, M. Lazzeri, M. Marsili, N. Marzari, F. Mauri, N. L. Nguyen, H.-V. Nguyen, A. Otero-de-la-Roza, L. Paulatto, S. Poncé, D. Rocca, R. Sabatini, B. Santra, M. Schlipf, A. P. Seitsonen, A. Smogunov, I. Timrov, T. Thonhauser, P. Umari, N. Vast, X. Wu, and S. Baroni, Advanced capabilities for materials modelling with QUANTUM ESPRESSO, *J. Phys.: Condens. Matter* **29**, 465901 (2017)..
- [88] P. Giannozzi, O. Baseggio, P. Bonfà, D. Brunato, R. Car, I. Carnimeo, C. Cavazzoni, S. De Gironcoli, P. Delugas, F. Ferrari Ruffino, A. Ferretti, N. Marzari, I. Timrov, A. Urru, and S. Baroni, QUANTUM ESPRESSO toward the exascale, *J. Chem. Phys.* **152**, 154105 (2020).
- [89] D. R. Hamann, Optimized norm-conserving Vanderbilt pseudopotentials, *Phys. Rev. B* **88**, 085117 (2013).
- [90] Z. Han, X. Yang, W. Li, T. Feng, and X. Ruan, FourPhonon: an extension module to ShengBTE for computing four-phonon scattering rates and thermal conductivity, *Comput. Phys. Commun.* **270**, 108179 (2022).
- [91] Ph. Lambin and J. P. Vigneron, Computation of crystal Green's functions in the complex-energy plane with the use of the analytical tetrahedron method, *Phys. Rev. B* **29**, 3430 (1984).
- [92] Q. Zheng, C. Li, A. Rai, J. H. Leach, D. A. Broido, and D. G. Cahill, Thermal conductivity of GaN, ⁷¹GaN, and SiC from 150 K to 850 K, *Phys. Rev. Mater.* **3**, 014601 (2019).
- [93] L. Lindsay, D. A. Broido, and T. L. Reinecke, First-principles determination of ultrahigh thermal conductivity of boron arsenide: A competitor for diamond? *Phys. Rev. Lett.* **111**, 025901 (2013).
- [94] A. Jeżowski, P. Stachowiak, T. Plackowski, T. Suski, S. Krukowski, M. Boćkowski, I. Grzegory, B. Danilchenko, and T. Paszkiewicz, Thermal conductivity of GaN crystals grown by high pressure method, *Phys. Status Solidi B* **240**, 447 (2003).
- [95] S. Dagli, K. A. Mengle, and E. Kioupakis, Thermal conductivity of AlN, GaN, and Al_xGa_{1-x}N alloys as a function of composition, temperature, crystallographic direction, and isotope disorder from first principles, [arXiv:1910.05440](https://arxiv.org/abs/1910.05440).
- [96] A. I. Hochbaum, R. Chen, R. D. Delgado, W. Liang, E. C. Garnett, M. Najarian, A. Majumdar, and P. Yang, Enhanced thermoelectric performance of rough silicon nanowires, *Nature (London)* **451**, 163 (2008).
- [97] T. Wang, J. Carrete, N. Mingo, and G. K. H. Madsen, Phonon scattering by dislocations in GaN, *ACS Appl. Mater. Interfaces* **11**, 8175 (2019).
- [98] J. Dai and Z. Tian, Rigorous formalism of anharmonic atomistic Green's function for three-dimensional interfaces, *Phys. Rev. B* **101**, 041301(R) (2020).
- [99] G. Kudlek, J. Hollandt, N. Presser, J. Gutowski, D. R. Menke, M. Kobayashi, and R. L. Gunshor, Long-term stable thermally induced absorptive optical bistability in MBE-grown ZnSe epilayers, *Superlattices Microstruct.* **8**, 381 (1990).
- [100] Z. Guo, A. Verma, X. Wu, F. Sun, A. Hickman, T. Masui, A. Kurumata, M. Higashiwaki, D. Jena, and T. Luo, Anisotropic thermal conductivity in single crystal β -gallium oxide, *Appl. Phys. Lett.* **106**, 111909 (2015).
- [101] M. Slomski, N. Blumenschein, P. P. Paskov, J. F. Muth, and T. Paskova, Anisotropic thermal conductivity of β -Ga₂O₃ at elevated temperatures: Effect of Sn and Fe dopants, *J. Appl. Phys.* **121**, 235104 (2017).
- [102] R. A. Duncan, G. Romano, M. Sledzinska, A. A. Maznev, J.-P. M. Péraud, O. Hellman, C. M. Sotomayor Torres, and K. A. Nelson, Thermal transport in nanoporous holey silicon membranes investigated with optically induced transient thermal gratings, *J. Appl. Phys.* **128**, 235106 (2020).
- [103] Q. Hao, G. Chen, and M.-S. Jeng, Frequency-dependent Monte Carlo simulations of phonon transport in two-dimensional porous silicon with aligned pores, *J. Appl. Phys.* **106**, 114321 (2009).
- [104] A. J. Schmidt, X. Chen, and G. Chen, Pulse accumulation, radial heat conduction, and anisotropic thermal conductivity in pump-probe transient thermoreflectance, *Rev. Sci. Instrum.* **79**, 114902 (2008).
- [105] C. Nenstiel, M. Bügler, G. Callsen, F. Nippert, T. Kure, S. Fritze, A. Dadgar, H. Witte, J. Bläsing, A. Krost, and A. Hoffmann, Germanium—the superior dopant in n-type GaN, *Phys. Status Solidi RRL* **9**, 716 (2015).
- [106] N. H. Protik and D. A. Broido, Coupled transport of phonons and carriers in semiconductors: A case study of n-doped GaAs, *Phys. Rev. B* **101**, 075202 (2020).
- [107] N. H. Protik and B. Kozinsky, Electron-phonon drag enhancement of transport properties from a fully coupled *ab initio* Boltzmann formalism, *Phys. Rev. B* **102**, 245202 (2020).
- [108] J. Zhou, B. Liao, B. Qiu, S. Huberman, K. Esfarjani, M. S. Dresselhaus, and G. Chen, *Ab initio* optimization of phonon drag effect for lower-temperature thermoelectric energy conversion, *Proc. Natl. Acad. Sci. USA* **112**, 14777 (2015).
- [109] B. Liao, B. Qiu, J. Zhou, S. Huberman, K. Esfarjani, and G. Chen, Significant reduction of lattice thermal conductivity by the electron-phonon interaction in silicon with high carrier concentrations: A first-principles study, *Phys. Rev. Lett.* **114**, 115901 (2015).
- [110] J.-Y. Yang, G. Qin, and M. Hu, Nontrivial contribution of Fröhlich electron-phonon interaction to lattice thermal conductivity of wurtzite GaN, *Appl. Phys. Lett.* **109**, 242103 (2016).

- [111] D.-S. Tang, G.-Z. Qin, M. Hu, and B.-Y. Cao, Thermal transport properties of GaN with biaxial strain and electron-phonon coupling, *J. Appl. Phys.* **127**, 035102 (2020).
- [112] A. Muthukunil Joseph and B. Cao, Electron heat source driven heat transport in GaN at nanoscale: Electron-phonon Monte Carlo simulations and a two temperature model, *Materials* **15**, 1651 (2022).
- [113] D.-S. Tang and B.-Y. Cao, Phonon thermal transport and its tunability in GaN for near-junction thermal management of electronics: A review, *Int. J. Heat Mass Transfer* **200**, 123497 (2023).
- [114] J. Ciers, M. A. Bergmann, F. Hjort, J.-F. Carlin, N. Grandjean, and Å. Haglund, Smooth GaN membranes by polarization-assisted electrochemical etching, *Appl. Phys. Lett.* **118**, 062107 (2021).